Journal of Geophysical Research: Earth Surface

RESEARCH ARTICLE
10.1029/2017JF004527

Key Points:
- Density-driven flows affect the long-term morphodynamic evolution of estuaries by enhancing near-bed flood dominance
- The combined effect of baroclinicity and Coriolis acceleration tends to promote cross-channel bathymetric asymmetry
- Three-dimensional process-based numerical models accounting for salinity variations resemble bathymetric and hydrodynamic features observed in estuaries

Correspondence to:
M. Olabarrieta,
maitane.olabarrieta@essie.ufl.edu

Citation:
Olabarrieta, M., Geyer, W. R., Coco, G., Friedrichs, C. T., & Cao, Z. (2018). Effects of density-driven flows on the long-term morphodynamic evolution of funnel-shaped estuaries. *Journal of Geophysical Research: Earth Surface*, *123*, 2901–2924. https://doi.org/10.1029/2017JF004527

Received 19 OCT 2017
Accepted 2 AUG 2018
Accepted article online 13 OCT 2018
Published online 14 NOV 2018

Effects of Density-Driven Flows on the Long-Term Morphodynamic Evolution of Funnel-Shaped Estuaries

Maitane Olabarrieta[1], W. Rockwell Geyer[2], Giovanni Coco[3], Carl T. Friedrichs[4], and Zhendong Cao[1]

[1]Civil and Coastal Engineering Department, ESSIE, University of Florida, Gainesville, FL, USA, [2]Applied Ocean Physics and Engineering, Woods Hole Oceanographic Institution, Woods Hole, MA, USA, [3]School of Environment, The University of Auckland, Auckland, New Zealand, [4]Virginia Institute of Marine Science, College of William and Mary, Williamsburg, VA, USA

Abstract Subtidal flows driven by density gradients affect the tide-averaged sediment transport in estuaries and, therefore, can influence their long-term morphodynamic evolution. The three-dimensional Coupled Ocean-Atmosphere-Wave-Sediment Transport modeling system is applied to numerically analyze the effects of baroclinicity and Earth's rotation on the long-term morphodynamic evolution of idealized funnel-shaped estuaries. The morphodynamic evolution in all the analyzed cases reproduced structures identified in many tide-dominated estuaries: a meandering region in the fluvial-tidal transition zone, a tidal maximum area close to the head, and a turbidity maxima region in the brackish zone. As the morphology of the estuaries evolved, the tidal propagation (including its asymmetry), the salinity gradient, and the strength of subtidal flows changed, which reflects the strong bathymetric control of these systems. The comparison with barotropic simulations showed that the three-dimensional structure of the flow (induced by density gradients) has leading order effects on the morphodynamic evolution. Density gradient-driven subtidal flows (1) promote near-bed flood dominance and, consequently, the import of sediment into the estuary, (2) accelerate the morphodynamic evolution of the upper/middle estuary, (3) promote a more concave shape of the upper estuary and reduce the ebb-tidal delta volume, and (4) produce an asymmetric bathymetry and inhibit the formation of alternate bars that would form under barotropic conditions. This latter effect is the consequence of the combined effect of Earth's rotation and baroclinicity.

1. Introduction

Estuaries are transgressive coastal environments at the mouth of rivers that receive sediment from both fluvial and marine sources and that contain facies influenced by tides, wind waves, and fluvial processes (Dalrymple, 2006). From a morphological perspective, estuaries consist of a combination of channels, shoals, tidal flats, and vegetated areas (Perillo, 1995). Estuaries are some of the most biologically productive (e.g., Robb, 2014) and the most threatened ecosystems on Earth (Kennish, 2002). Sea level, river discharge, wave climate, and storm (intensity and frequency) variations due to climate change are expected to impact and modify the shape of the estuaries and the associated ecosystems. Nonetheless, our understanding of medium (greater than decade) and long-term (greater than century) estuarine morphodynamic development is still limited, and further research is needed to understand the natural state of estuaries and their response to external forcing conditions.

The morphology of an estuary is primarily controlled by river flow, tides, waves, and sediment supply (e.g., de Swart & Zimmerman, 2009). Tide-dominated estuaries generally show a funnel-shaped geometry (Dronkers, 2017; Fagherazzi & Furbish, 2001; Myrick & Leopold, 1963; Rinaldo et al., 2004; Wright et al., 1973). This landward reduction of the cross-sectional area is a consequence of the reduction of the tidal flux (Myrick & Leopold, 1963). Unless the estuary is in equilibrium (Zhou et al., 2017), sediment transport is usually different between flood and ebb tides. This generates a tidal asymmetry in sediment transport, which in turn triggers morphological evolution. The sediment transport asymmetry can result from different processes, such as the generation of overtides, river outflow, gravitational circulation, eddy viscosity-shear covariance, lateral secondary flows, barotropic subtidal flows, and wind waves. For example, as the tidal wave propagates along an estuary, it can deform or distort due to nonlinear effects (e.g., Friedrichs & Aubrey, 1988). If tidal flats are not fully developed, the asymmetry promotes flood dominance and, therefore, a tendency of the estuary to

fill in with sediment. The response of the estuary is to develop tidal flats that will increase frictional effects close to high tide and deeper main channels that will intensify tidal currents during the ebb. As explained by Fortunato and Oliveira (2005), estuaries with extensive tidal flats can be ebb dominated (e.g., Fortunato et al., 1999), whereas the absence of tidal flats favors flood dominance (Lanzoni & Seminara, 2002). Overall, the evolving morphology tends to reduce flood dominance. Subtidal flows due to the river discharge, gravitational circulations, tidal stresses, or return flows can also contribute to the tide-averaged sediment transport.

Medium- and long-term estuarine morphodynamics have been analyzed with different approaches, including physical (e.g., Iwasaki et al., 2013; Kleinhans et al., 2012; Reynolds, 1889, 1890, 1891; Stefanon et al., 2010, 2012; Tambroni et al., 2005; Vlaswinkel & Cantelli, 2011) and numerical modeling (e.g., Ganju et al., 2009; Hibma et al., 2003a, 2003b, 2004; Lanzoni & Seminara, 2002; Marciano et al., 2005; Schuttelaars & de Swart, 1996, 1999; van der Wegen, 2013; Van der Wegen et al., 2010; Van Maanen, Coco, & Bryan, 2013; Van Maanen, Coco, Bryan, & Friedrichs, 2013; Zhou et al., 2014). As emphasized by Coco et al. (2013), laboratory experiments are able to reproduce naturally observed morphological features, but shortcomings related with scaling remain. Moreover, most of the physical experiments showed an erosional tendency of the estuary, whereas many natural estuarine systems are flood dominated (transgressive), and, therefore, depositional. None of these physical models considered the effects of density-driven flows.

During the last decade, remarkable progress has been made on the long-term morphodynamic modeling of estuarine systems. In most of the studies, a depth-averaged 2DH model simplification is adopted for the hydrodynamics (e.g., Hibma et al., 2003b; Marciano et al., 2005; Van der Wegen & Roelvink, 2008; Van Maanen et al., 2015). The riverine influence has been included in recent studies (e.g., Canestrelli et al., 2014; Guo et al., 2014; Zhou et al., 2014), but density variations, and, therefore, density gradient-driven flows, are usually disregarded. Under these circumstances (vertically uniform flow) the total sediment transport is usually computed using a simplified formula (Engelund & Hansen, 1967), in which the total load is proportional to a certain power of the depth-averaged velocity (e.g., Guo et al., 2014; Van Maanen et al., 2013; Zhou et al., 2014). In a few cases, density-driven circulation has been included in two-dimensional width-averaged models of equilibrium estuarine sediment dynamics in well-mixed tidal estuaries (e.g., Chernetsky et al., 2010; Dijkstra et al., 2017). However, sediment transport is rarely solved using a three-dimensional advection-diffusion equation. Despite the relevance of the density-driven flows and Earth's rotation in nutrient, pollutant, larvae, and sediment dispersal in estuaries (e.g., Geyer & MacCready, 2014; MacCready & Geyer, 2010), these processes are hardly ever accounted for when modeling estuarine morphodynamics.

The aim of this study is to analyze the effects of density-driven circulation and Earth's rotation on the long-term morphodynamics of tide-dominated funnel-shaped estuaries. Although not specifically dealing with morphodynamics, Huijts et al. (2006, 2009, 2011) proposed two physical mechanisms associated with the Coriolis acceleration and cross-channel density gradients. Both mechanisms could affect estuarine morphodynamic evolution by contributing to the lateral accumulation of sediment in tide-dominated estuaries. According to these studies, the effect of Coriolis on tidal currents would produce lateral entrapment of sediment on the right slope of the channel (looking up-estuary in the Northern Hemisphere). On the other hand, secondary flows driven by density gradients would produce sediment trapping in the region of freshwater (on the left side in the Northern Hemisphere). At low vertical Ekman numbers ($E < 0.02$) the Coriolis mechanism is dominant, whereas at larger vertical Ekman numbers ($E > 0.02$) density gradient-driven secondary flow dominates the lateral entrapment of sediment. The vertical Ekman number (E) is given by the expression $E = A_z/(fH^2_{max})$ where A_z is the vertical eddy viscosity coefficient, f represents the Coriolis parameter, and H_{max} is the maximum water depth along a cross-channel section. These pioneering studies provide insightful information on the mechanisms of sediment trapping along the flanks of the channels, but they do not fully consider the interdependency of the density field and the Coriolis acceleration. In the study by Huits et al. (2006, 2009), the cross-channel salinity gradient is prescribed, whereas in real estuaries the cross-channel density variations can be affected by the secondary flows themselves, most notably geostrophic adjustment. Therefore, the effects of specified lateral density gradients can only represent the effect of the Coriolis acceleration indirectly. Moreover, these models do not include nonlinear morphodynamic feedbacks.

Here we consider an idealized estuary to analyze the role of Earth's rotation and density-driven flows on the long-term morphodynamic evolution (~100–200 years), including their interdependency and the possible nonlinear morphodynamic feedbacks. The analysis focuses on the main processes that affect the

sediment fluxes in the absence of wind and wind waves: tidal distortion (generation of overtides) and subtidal flows.

2. Numerical Model Description and Setup

The coupled ROMS (Regional Ocean Modeling System) and CSTMS (Community Sediment Transport Modeling System) presented by Warner et al. (2008) is applied in an idealized funnel-shaped generic estuary. ROMS is a three-dimensional, free-surface, terrain-following numerical model that solves finite difference approximations of the Reynolds-Averaged Navier-Stokes equations using the hydrostatic and Boussinesq assumptions (Chassignet et al., 2000; Haidvogel et al., 2000) with a split-explicit time-stepping algorithm (Haidvogel et al., 2008; Shchepetkin & McWilliams, 2005). We use the generic length-scale method (Umlauf & Burchard, 2003) as implemented by Warner et al. (2005) to represent the vertical turbulence. In this method the bottom shear and surface shear stresses are included as boundary conditions.

The total sediment transport in ROMS is computed as the sum of suspended and bed load transport. Different sediment classes can be defined in the model. The three-dimensional advection-diffusion equation with the following additional source/sink term is used to transport the suspended sediment concentration (Warner et al., 2008):

$$C_{\text{source}} = -\frac{\partial w_s C}{\partial s} + E_s \tag{1}$$

and

$$E_s = E_0(1-\phi)\frac{|\tau_b| - |\tau_{ce}|}{|\tau_{ce}|} \tag{2}$$

where s is the vertical direction (s represents the sigma-vertical coordinate used in ROMS and ranges from -1 at the bottom to 0 at the surface), w_s the vertical settling velocity (m/s; positive upward), E_s the erosion source (kg $\cdot$ m^2 $\cdot$ s), E_o the bed erodibility rate (kg $\cdot$ m^2 $\cdot$ s), ϕ the sediment porosity, τ_b the bottom shear stress (N/m^2) with the expression given in equation (3), and τ_{ce} the critical shear stress for sediment erosion (N/m^2). Slope-dependent bed load is included using Soulsby and Damgaard (2005) and Lesser et al. (2004) formulations contained in Coupled Ocean-Atmosphere-Wave-Sediment Transport (COAWST) for pure currents (Warner et al., 2008). Although both bed load and suspended load are considered in the present study, suspended sediment transport is dominant over the bed load in all the analyzed cases. The bed load component of COAWST is retained in these computations to prevent sharp morphologic instabilities (cf. the bed slope diffusion term in the models of Schuttellaars and de Swart, 1996, and Van Maanen, Coco, & Bryan, 2013; Van Maanen, Coco, Bryan, & Friedrichs, 2013).

Sediment flux divergence is used to determine changes of sediment mass in the bed at each grid cell. Bed level (z_b) changes are computed every time step by the Exner equation:

$$(1-\phi)\left(\frac{\partial z_b}{\partial t}\right) + \left(\frac{\partial q_{b,x}}{\partial x}\right) + \left(\frac{\partial q_{b,y}}{\partial y}\right) = -\frac{C_{\text{source},b}}{\rho_s} \tag{3}$$

where t represents time, x and y the horizontal coordinates, ρ_s the sediment density, and $C_{\text{source},b}$ the suspended sediment concentration source/sink evaluated at the bottom (sediment resuspension deposition). A constant morphological scale factor that multiplies the erosion and deposition rates and the bed load flux by 50 is used to accelerate the morphodynamic response. Roelvink (2006) presented an overview of different morphodynamic acceleration methods. In the current model the acceleration factor is considered constant along the numerical simulations and is applied at each time step. For a more detailed description of the sediment transport model, the reader is referred to Warner et al. (2008).

The geometry of the generic three-dimensional estuary, its sediment characteristics, and the considered boundary conditions are representative of the types of estuaries along the northeast coast of the United States, such as the Hudson River, the York River, or the James River estuaries. This generic idealized estuary is funnel shaped with a maximum width of 1.2 km at the mouth (Figure 1, top). The initial bathymetry has a symmetric Gaussian shape in the cross-channel direction. The water depth is maximum (~15 m) along the thalweg and decreases to 2 m in the flanks of the estuary. The 0.1-m amplitude

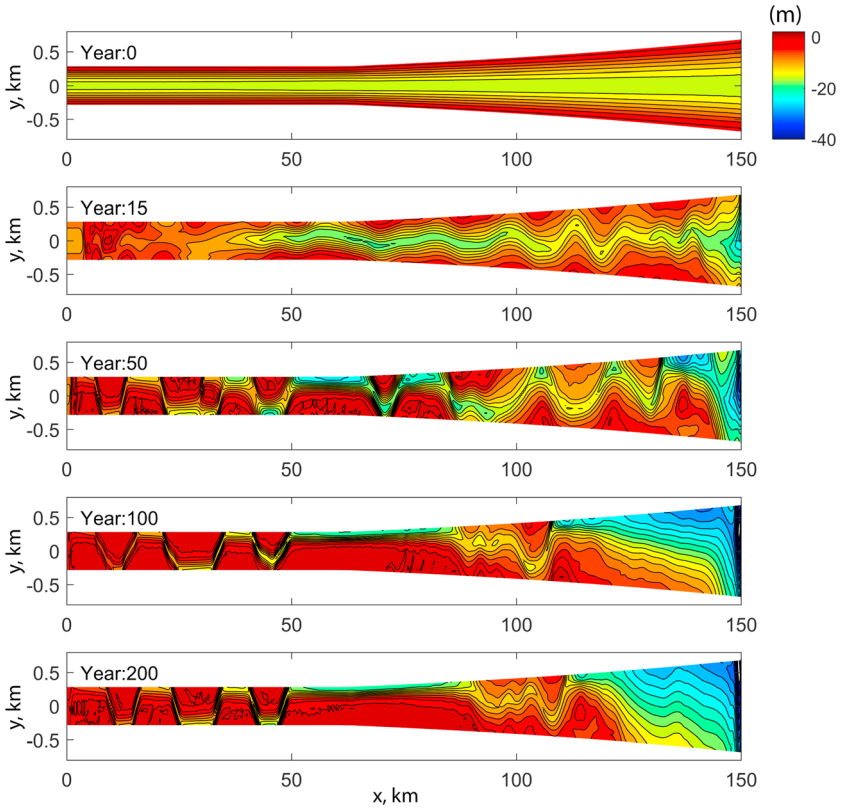

Figure 1. Temporal evolution of the bathymetry over 200 years (Q = 150 m^3/s, TR = 1.5 m, w_s = 0.6 mm/s, and latitude = 41°N).

random perturbations are imposed to the initial bathymetry. Offshore of the mouth of the estuary, the continental shelf is characterized by a constant bottom slope of 0.0005. The horizontal numerical grid is curvilinear. The cross-channel horizontal resolution is 25 m at the thalweg and increases exponentially to 837 m at the edges of the grid. In the along-channel direction, inside the estuary the grid resolution is constant and equal to 200 m. The grid resolution decreases exponentially from the mouth of the estuary to the offshore open boundary, where the grid resolution is 875 m. The vertical flow structure is solved with 10 equally spaced sigma-vertical layers.

At the offshore boundary a symmetric M_2 tidal wave and a constant salinity of 35 psu are imposed. The temperature is assumed to be constant (15 °C). At the landward boundary a freshwater discharge is specified. Three tidal ranges (TR = 0.7, 1, and 1.5 m) and five river discharges (Q= 50, 100, 150, 250, and 350 m^3/s) are considered. To isolate and ascertain the effects of density gradients, a second set of experiments is performed by assuming no salinity variations along the estuary. The effect of Coriolis acceleration is analyzed by considering the same idealized estuary but located in five different latitudes (41°N, 31°N, equator, 31°S, and 41°S). Our base case is located at 41°N (the location of the Hudson Estuary). Most of the numerical experiments assume a single-sediment class equivalent to medium silt (or flocculated estuarine mud) with the fall velocity (w_s) equal to 0.6 mm/s and the critical shear stress for erosion of 0.05 Pa. To analyze the sensitivity of the model to the sediment characteristics, one more sediment class (fine sand) with fall velocity of 5.0 mm/s and a critical shear stress of 0.1 Pa is considered. The erosion rate for both sediment classes is $1.0 \cdot 10^{-4}$ Kg $\cdot$ m^2 $\cdot$ s. These values have been chosen based on Ralston et al. (2012) in application to the Hudson River estuary. The initial bed layer thickness is considered equal to 50 m in all the cases. At the river side a closed boundary and at the ocean boundaries a zero gradient condition are imposed for the sediments. Although a closed boundary at the river side might not be a realistic representation of what happens in nature, it allows us to ascertain how the sediment in the system is distributed as a function of the external forcing conditions. The ocean boundaries are in higher water depths and sediment transport rates in this area are negligible.

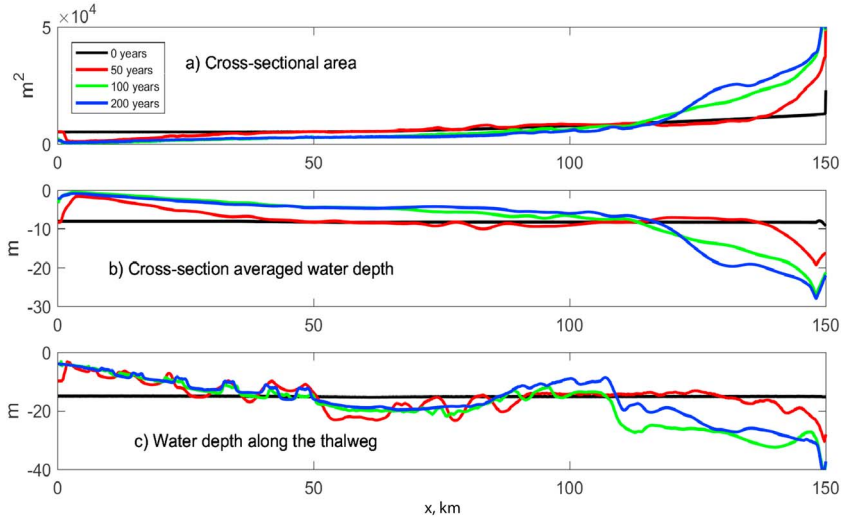

Figure 2. Temporal evolution of (a) cross-channel sectional area, (b) cross-channel averaged water depth, and (c) thalweg water depth along the estuary (Q = 150 m^3/s, TR = 1.5 m, w_s = 0.6 mm/s, and latitude = 41°N).

Although most of the simulations shown in this manuscript are representative of microtidal estuaries (tidal range $<$ 2 m), we complimented the analysis by considering one more idealized estuary with different geometry and boundary conditions. The goal of this additional simulation is to analyze if the results for microtidal estuaries may be applicable to other types of estuaries with different stratification and tidal range (mesotidal) conditions.

Each numerical simulation has a spin-up time of 60 days before considering the morphodynamic evolution. After the salinity gradient has stabilized, the morphodynamic module is switched on, and each simulation is run for 200 years (i.e., 4 years of hydrodynamic time stepping with a morphodynamic acceleration factor of 50). Hydrodynamic fields for a tidal cycle are stored after every 4 years (in accelerated time) to analyze the evolution of the hydrodynamics and sediment transport as the morphology evolves. Because of the simplifications assumed in these numerical simulations (e.g., consolidation effects and time-varying boundary conditions are not accounted for), the actual temporal evolution timescale is not well constrained, and it should be thought of as a relative timescale.

3. Results

3.1. Morphodynamic Evolution

In this section we provide a detailed description of the temporal evolution of one specific case that includes density gradients (Q = 150 m^3/s, tidal range = 1.5 m, latitude = 41°N, and w_s = 0.6 mm/s).

3.1.1. Bathymetric Evolution

Four different phases can be distinguished along the morphodynamic evolution (Figures 1 and 2). During Phase 1 (0–15 years) the observed bathymetric changes are maximal because the initial morphology is far from the equilibrium. Sediment transport capacity is greatest in the mid-estuary and diminishes toward the head. Consequently, the central part of the estuary erodes, while close to the head, the formation of a bar is observed. Intertidal flats start to develop in the upper-middle estuary, and the growth of some instabilities or bars can be identified. Due to the preimposed funnel shape, the initial cross-sectional area decreases from the mouth to the head as a consequence of the width reduction (from 1,200 m at the mouth to 500 m at the head). As the morphology evolves, the cross-sectional area increases close to the mouth and decreases at the head (Figure 2a). During this phase the cross-sectional area changes are less than 50%. The cross-channel averaged water depth shows the initial formation of a bar in the upper estuary. Offshore of the estuary mouth, water depths decrease due to the formation of an ebb-tidal delta.

During Phase 2 (~15 to 50 years), the bar that formed close to the head evolves into meanders and point bars. These represent morphological features characteristic of river systems (e.g., Seminara, 2010). The orientation

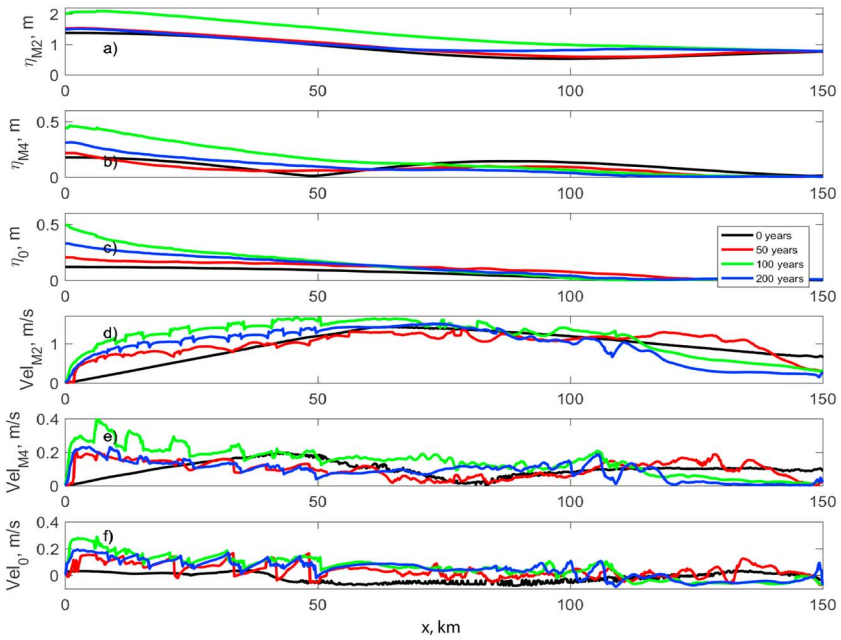

Figure 3. Temporal evolution of (a) M_2 free-surface elevation amplitude, (b) M_4 free-surface elevation amplitude, (c) mean water level, (d) depth-averaged M_2 velocity amplitude, (e) depth-averaged M_4 velocity amplitude, and (f) depth-averaged subtidal flow along the thalweg (Q = 150 m^3/s, TR = 1.5 m, w_s = 0.6 mm/s, and latitude = 41°N). Positive velocities are directed toward the ocean.

of the bars, slightly headward during this period, is indicative of the direction of the subtidal sediment transport (Tambroni et al., 2017).

In the middle-lower estuary, the resonant growth of the main oscillation modes of the system results in the formation of a well-developed alternate bar system. In the upper estuary, the cross-sectional area decreases by more than 90% (Figure 2a); the cross-section averaged water depth decreases to almost 2 m (Figure 2b). The sediment accreted at the upper estuary is not balanced by the amount of sediment eroded in the lower region. Since there is no sediment imported from the river boundary, this sediment is imported from the estuary mouth.

During Phase 3 (~50 to 100 years), the meander system located close to the head becomes more symmetric. This might indicate that the subtidal sediment transport has decreased or changed direction due to the formation of intertidal areas. The alternate bars that formed during Phase 2 in the middle and lower estuary start to disappear. Instead, a longitudinally more homogeneous channel-flat system is developed. The cross-channel asymmetry of the bathymetry is one of the most distinctive characteristics of the morphology at this stage: lateral shallows/tidal flats and the deeper main channel have developed in the left and right sides (looking into the estuary), respectively. The cross-sectional area has increased about 5 times the initial value close to the mouth and has reduced more than half at the head (Figure 2a). The cross-channel averaged bathymetry has developed a concave profile characteristic of tide-dominated estuaries (Figure 2b). The cross-channel averaged water depth increases in the mouth and middle estuary and reduces to almost 1.5 m close to the head.

After 100 years three different regions can be identified along the estuary: (1) the upper estuary, which is characterized by a meandering system with a shallow and narrow (<50-m) main channel flanked by tidal flats with elevations close to the high-tide level; (2) the middle estuary, which is characterized by a straight and asymmetric cross section, with the main channel in the right and intertidal areas in the left; and (3) the lower estuary, which is characterized by an asymmetric cross section that also shows along-channel bars.

During Phase 4 (>100 years) the meanders and point bar system located at the head start to erode and the lower estuary becomes deeper. The observed morphological changes are weaker than previously observed

changes. During the first three phases the estuary is transgressional and imports sediment for the open ocean. In the last phase the estuary has started to transition to a sediment exporting/progading system.

3.1.2. Hydrodynamic Evolution

The bathymetric control on the tidal propagation is shown in Figure 3. Initially, due to the dominance of friction over the convergence of the estuary, the M_2 tidal amplitude decreases from the mouth to the middle part of the estuary (until ~90 km from the head). The amplitude of the M_2 velocity along the thalweg is maximum (~1.2 m/s) in the central region (~60 km from the head). Due to the reflection of the tide at the head, an increase of the elevation and reduction of velocity amplitudes is observed toward the head. As the morphology evolves, the M_2 amplitude dissipation decreases in the lower estuary (especially after year 50). Due to the reduction of the cross-sectional area close to the head, the increase of the convergence of the estuary enhances the tidal amplification to ~2.1 m. In the last phase of the evolution, because water depths at the upper estuary slightly increase, the amplification is reduced to ~1.5 m. Initially, the relative amplitude of the first overtide M_4 (Figure 3b) is maximum in the region where the M_2 amplitude is minimum (middle of the estuary) and minimum at 50 km from the head. As the morphology evolves, the M_4 elevation amplitude starts to show a progressive increase from the mouth toward the head. The maximum values (~0.5 m) are obtained after 100 years of evolution, when the head is shallowest. In the last phase (100–200 years) the maximum amplitude of the M_4 decreases to 0.3 m. The mean water level (Figure 3c) shows a progressive increase through the estuary in all the evolution stages. Nonetheless, the maximum water level (0.5 m) is observed after 100 years of evolution and then decreases to 0.35 m.

With respect to the velocity amplitudes, the morphodynamic evolution produces a more homogeneous M_2 velocity distribution along the estuary, except in the lower estuary, where it decreases. The maximum velocities in the central and head of the estuary are obtained after 100 years of evolution, when the estuary (especially the upper estuary) is shallowest (Figure 3d). The M_4 velocity amplitude shows initially a maximum located 50 km from the head (Figure 3e). This, together with the minimum elevation magnitude, indicates the presence of a node. As the bathymetry changes, the node disappears, and instead, the more homogeneous distribution is observed (although the presence of the alternate bars and meanders produce along-channel variations in the amplitude). The maximum values (~0.4 m/s) are obtained at the head, after 100 years of evolution. The most noticeable changes in the depth-averaged subtidal flows (Figure 3f) occur close to the head, where the river-induced velocities increase from almost 0.05 to 0.2 m/s due to the reduction of the cross-sectional area. After 50 years of evolution, depth-averaged subtidal flows are positive all along the thalweg of the estuary. After 100 years, in the lower estuary ($x >$ ~110 km), the velocities along the thalweg change direction and flow toward the head.

Overall, as the bathymetry changes, the elevation amplitudes (M_2, M_4, and mean) tend to show a progressive increase from the mouth toward the head. Maximum amplitudes are observed after 100 years of evolution, when the convergence of the estuary is maximum. There is also a tendency for the velocity amplitudes to show more homogeneous values along the estuary, although the M_4 velocity and the subtidal flow show an increase toward the head. If we add the M_2 and the M_4 tidal components, the maximum tidal velocities occur in the region where the maximum M_2 elevations are observed.

The normalized tidal distortion υ is defined as the product of the relative M_4 velocity amplitude (U_{M4}/U_{M2}) and the cosine of the phase-lock between the main harmonic and the first overtide($2\phi_{M2,\,U} - \phi_{M4,\,U}$):

$$\upsilon = \frac{U_{M4}}{U_{M2}} \cos\left(2\phi_{M2,U} - \phi_{M4,U}\right) \tag{4}$$

The amplitudes (U_{M2}, U_{M4}) and phases ($\phi_{M2,\,U}, \phi_{M4,\,U}$) correspond to the along-estuary components (the cross-estuary velocity components are 1 order of magnitude smaller). υ is indicative of the strength and direction of the flood- or ebb-dominant tidal distortion. Velocity amplitudes and the phases are depth averaged, and therefore, υ represents the overall (depth-averaged) tidal distortion.

Initially, strong flood dominance is observed in the shallow flanks of the mid-estuary (Figure 4). The deeper channels are ebb dominant, but the distortion is weak (close to zero). The upper/lower estuary is flood/ebb dominant. The tidal distortion evolves toward symmetric tidal condition (almost null tidal distortion) in the mid-estuary as the morphology evolves. Conversely, in the upper estuary the flood dominance

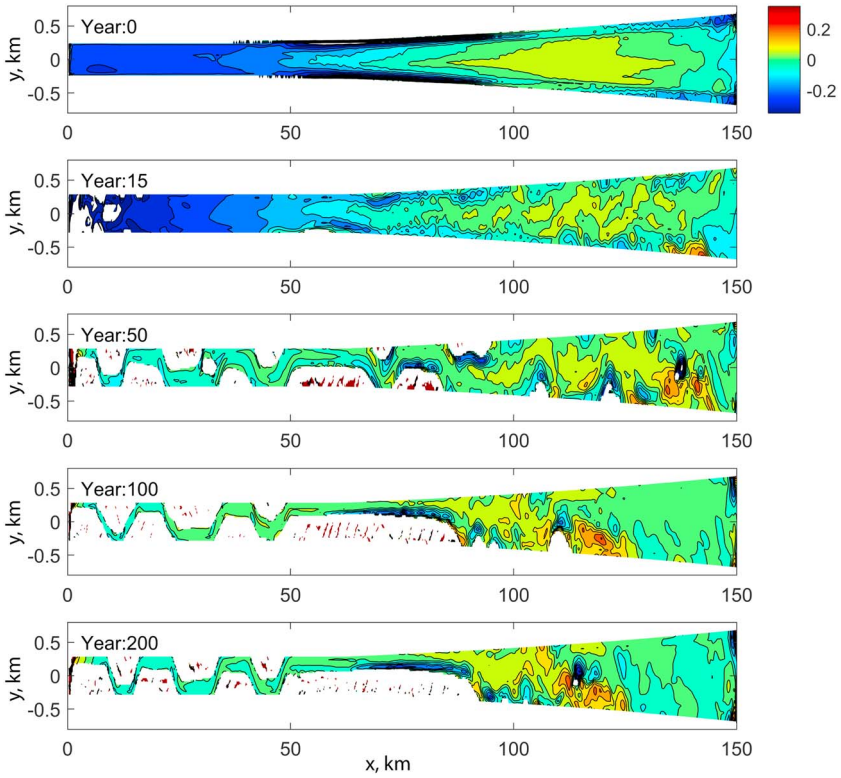

Figure 4. Temporal evolution of the normalized tidal distortion parameter υ (Q = 150 m^3/s, TR = 1.5 m, w_s = 0.6 mm/s, and latitude = 41°N). The velocity amplitudes are representative of the depth-averaged tidal velocities. Positive values indicate ebb dominance, whereas negative values indicate flood dominance. The unshaded areas in (b) to (e) are intertidal.

increases initially; once the meanders reach their maximum development, and the cross-sectional area of the upper estuary decreases to a minimum value, tidal distortion switches toward ebb dominance. Notice that initially, even in the absence of tidal flats, in the middle-lower estuary the tidal distortion produces ebb dominance. This may be a consequence of tidal straining of the salinity field and associated asymmetries in bottom stress interacting nonlinearly with M_2 velocity.

Given the strength of freshwater discharge relative to the tidal forcing, this should be a partially mixed estuary (Geyer & MacCready, 2014). Initially, the salinity gradient extends from the mouth up to 40 km from the head. The resulting density gradients drive the typical three-dimensional estuarine circulation, characterized by an outflow of freshwater in the upper water column and an inflow of saltier water at the bottom (Figure 5a). In the shallower flanks of the estuary, a net outflow is observed, especially in the middle and lower estuary (not shown). The intensity of the bottom subtidal flow is maximum (~0.17 m/s) along the thalweg in the mid/upper estuary (60 to 90 km from the head). Near the head, the river flow is initially weak (~0.05 m/s). As the morphology evolves, the upper cross-sectional area decreases and the river velocity increases up to 0.3 m/s. Consequently, the region dominated by the river, where the flow is vertically homogeneous, extends toward the ocean (Figure 5a). Since the river velocity and the tidal propagation evolve as a consequence of the bathymetric changes, the along-estuary salinity gradient and the stratification also respond to these changes. The maximum along-channel density gradients are observed after 200 years of evolution (Figure 5b). During this interval, the river-dominated region has achieved its maximum extent, and the erosion of the mouth area allows the salty water to penetrate farther into the estuary. This increases the salinity gradient and reduces the *effective* length of the estuary.

In all the stages of evolution, an estuarine turbidity maximum (ETM) is observed (Figure 5c). Initially, the bottom suspended sediment concentration (SSC) is almost constant along the thalweg, except at the head, where the concentration decreases. The surface SSC depends on the strength of the stratification. The less stratified the water column, the more SSC reaches the surface. The initial maximum SSC is observed 50 km from the head, starting at the brackish zone. As the bathymetry changes and the river velocity increases,

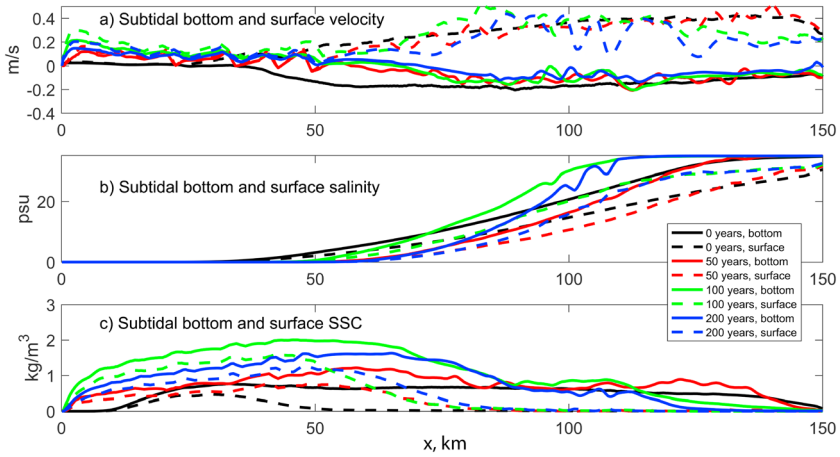

Figure 5. Temporal evolution of bottom model cell (continuous) and surface model cell (discontinuous) (a) subtidal flow, (b) subtidal salinity, and c) subtidal suspended sediment concentration along the thalweg (Q = 150 m^3/s, TR = 1.5 m, w_s = 0.6 mm/s, and latitude = 41°N).

the SSCs at the bottom and at the surface increase and move toward the ocean, following the salinity intrusion limit or the transition between fresh (and vertically homogeneous) and saltier (vertically sheared) flows. Maximum SSC values (>2 kg/m^3) are observed at 100 years of evolution, after which maximum values decrease to ~1.1 kg/m^3. The maximum SSC values correspond to the period when the tidal distortion in the head of the estuary switches to ebb dominance, that is, when river velocities are maximum. After 100 years, the tidal velocities, sum of M_2 and M_4, are maximum as well. At this stage, the cross-sectional area in the upper estuary is minimum, the convergence maximum, and the tidal and river velocities are maximum as well. Consequently, the capacity for resuspension of sediment is maximum. In the region affected by the salinity gradients, the stratification limits the vertical extent of the suspended sediment concentration.

3.1.3. Eulerian Sediment Transport Proxy

Sanay et al. (2007) proposed an Eulerian subtidal sediment transport proxy, assuming that the instantaneous sediment transport is proportional to the cube of the instantaneous near-bottom velocities (Bagnold, 1966; Gräwe et al., 2014; Ralston & Geyer, 2009). Following the same approach, we will utilize a proxy that assumes that the near-bottom instantaneous Eulerian sediment transport vector $\overrightarrow{q}_t$ is approximately proportional to the cube of the instantaneous near-bottom velocity vector $\overrightarrow{u_b}(t)$:

$$\overrightarrow{q}_t(t) = \alpha\left(\overrightarrow{u}_b(t)\cdot\left|\overrightarrow{u}_b(t)\right|^2\right) \tag{5}$$

The instantaneous velocities can be now decomposed into subtidal $\overrightarrow{u_{0,b}} = \left(U_{0,b}, V_{0,b}\right)$ and tidal components; considering that the tidal component can be decomposed into the main harmonic and first overtide,

$$\overrightarrow{u_{M2,b}} = \left(U_{M2,b}\cos\left(\frac{2\pi}{T_{M2}}t + \phi_{U,M2,b}\right), V_{M2,b}\cos\left(\frac{2\pi}{T_{M2}}t + \phi_{V,M2,b}\right)\right) \tag{6}$$

$$\overrightarrow{u_{M4,b}} = \left(U_{M4,b}\cos\left(\frac{2\pi}{T_{M4}}t + \phi_{U,M4,b}\right), V_{M4,b}\cos\left(\frac{2\pi}{T_{M4}}t + \phi_{V,M4,b}\right)\right) \tag{7}$$

where $U_{0,\,b}$ and $V_{0,\,b}$ represent the along-estuary and cross-estuary near-bottom subtidal flow components; T_{M2} and T_{M4} represent the period of the M_2 and M_4 tidal constituents (T_{M4} is half T_{M2}); $U_{M2,\,b}$ and $V_{M2,\,b}$ are the along-estuary and cross-estuary M_2 velocity amplitudes, respectively; and $\phi_{U,\,M2,\,b}$ and $\phi_{V,\,M2,\,b}$ are the phases of each tidal velocity component. The subscript b refers to near bottom. The amplitudes and phases of the M_4 component are represented in similar way but with the M_4 subscript. α (kg · s^2 · m^4) is a

proportionality coefficient dependent on the sediment characteristics. $\overrightarrow{q}_t$ is then averaged over the tidal cycle (denoted as $\langle\rangle$) resulting in the following expressions for the along-estuary $\langle q_t\rangle_x$ and cross-estuary $\langle q_t\rangle_y$ sediment transport:

$$\langle q_t\rangle_x = \alpha\left[\begin{array}{l}\left\{\begin{array}{l}U_{0,b}\left[\left(U_{0,b}{}^2+V_{0,b}{}^2\right)+\frac{1}{2}\left(3U_{M2,b}{}^2+V_{M2,b}{}^2\right)+\frac{1}{2}\left(3U_{M4,b}{}^2+V_{M4,b}{}^2\right)\right]+\\ V_{0,b}\left[U_{M2,b}V_{M2,b}\cos\left(\phi_{M2,U,b}-\phi_{M2,V,b}\right)+U_{M4,b}V_{M4,b}\cos\left(\phi_{M4,U,b}-\phi_{M4,V,b}\right)\right]\end{array}\right\}+\\ \left\{\begin{array}{l}U_{M4,b}\left[\frac{3}{4}U_{M2,b}{}^2\cos\left(-\phi_{M4,U,b}+2\phi_{M2,U,b}\right)+\frac{1}{4}V_{M2,b}{}^2\cos\left(\phi_{M4,U,b}-2\phi_{M2,V,b}\right)\right]+\\ \frac{1}{2}U_{M2,b}V_{M2,b}V_{M4,b}\cos\left(-\phi_{M4,V,b}+\phi_{M2,U,b}+\phi_{M2,V,b}\right)\end{array}\right\}\end{array}\right] \tag{8}$$

$$\langle q_t\rangle_y = \alpha\left[\begin{array}{l}\left\{\begin{array}{l}V_{0,b}\left[\left(U_{0,b}{}^2+V_{0,b}{}^2\right)+\frac{1}{2}\left(3V_{M2,b}{}^2+U_{M2,b}{}^2\right)+\frac{1}{2}\left(3V_{M4,b}{}^2+U_{M4,b}{}^2\right)\right]+\\ U_{0,b}\left[U_{M2,b}V_{M2,b}\cos\left(\phi_{M2,U,b}-\phi_{M2,V,b}\right)+U_{M4,b}V_{M4,b}\cos\left(\phi_{M4,U,b}-\phi_{M4,V,b}\right)\right]\end{array}\right\}+\\ \left\{\begin{array}{l}V_{M4,b}\left[\frac{3}{4}V_{M2,b}{}^2\cos\left(-\phi_{M4,V,b}+2\phi_{M2,V,b}\right)+\frac{1}{4}U_{M2,b}{}^2\cos\left(\phi_{M4,V,b}-2\phi_{M2,U,b}\right)\right]+\\ \frac{1}{2}V_{M2,b}U_{M2,b}U_{M4,b}\cos\left(-\phi_{M4,U,b}+\phi_{M2,V,b}+\phi_{M2,U,b}\right)\end{array}\right\}\end{array}\right] \tag{9}$$

This proxy neglects settling-lag effects and effects of stratification on suspended sediment concentration but provides a lowest-order indication of the relative magnitude of other contributions to net Eulerian transport. $\langle\overrightarrow{q_t}\rangle$ is composed by two main parts, indicated within braces in each equation (as in Sanay et al., 2007). The first term includes a purely subtidal and a nonlinear interaction term between the subtidal flow and the square of the tidal velocities. This component reflects the contribution of subtidal flows to the net sediment transport (barotropic and density driven); the second term includes the contribution of the tidal distortion. In all analyzed cases, the nonlinear interaction is at least an order of magnitude larger than the purely subtidal flow component. Since the first term depends on the existence of the subtidal flow, it will be referred as the subtidal flow contribution.

In the analyzed cases, the along-estuary velocities (the subtidal and tidal components) are 1 order of magnitude higher than the cross-channel components. Therefore, all the terms containing the square of the cross-estuary velocities can be neglected with respect to the terms proportional to square of the along-estuary components, resulting in the following expression:

$$\frac{\langle q_t\rangle_x}{\alpha} = \underbrace{U_{0,b}\left\{\left(U_{0,b}{}^2\right)+\frac{3}{2}\left(U_{M2,b}{}^2+U_{M4,b}{}^2\right)\right\}}_{\text{subtidal contribution = purely subtidal + non-linear interaction with tides}} + \underbrace{\left\{\frac{3}{4}U_{M4,b}U_{M2,b}{}^2\cos\left(2\phi_{M2,U.b}-\phi_{M4,U,b}\right)\right\}}_{\text{tidal distortion contribution}} \tag{10}$$

The normalized tidal distortion parameter υ, previously defined in equation (4), is the tidal distortion contribution (but instead of being evaluated at near the bed, it is calculated with the amplitudes and phases of the depth-averaged velocities) divided by $\frac{3}{4}U_{M2}^3$.

The application of the sediment transport proxy given by equation (10) to the model's bottom cell shows that the subtidal sediment transport along the thalweg is mainly driven by the subtidal flow and specifically by the density gradient-driven circulation (Figure 6). Only close to the head of the estuary (0–50 km) is tidal distortion dominant over the subtidal flow. Nonetheless, the sediment transport in this region is initially lower than in the rest of the estuary. As the upper estuary becomes shallower, the river velocity increases. After 50 years of evolution, there is still flood-directed tidal distortion influence, but the effect on the total sediment transport is weaker, since the river effect becomes dominant. At 50–60 km a subtidal flow convergence zone is observed. From 60 km to the mouth, the sediment transport along the thalweg is toward the head and is primarily driven

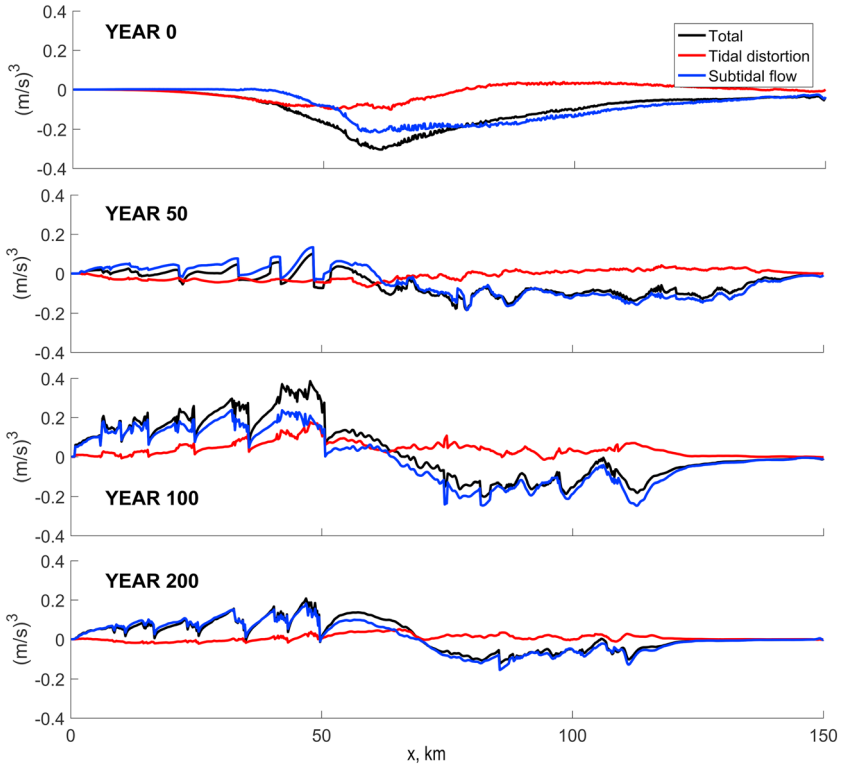

Figure 6. Temporal evolution of along-channel subtidal sediment transport proxies applied to the bottom model cell along the thalweg. Abrupt variations result from the along-estuary variation in morphology. Positive values indicate sediment transport proxy toward the ocean.

by the subtidal flow. After 100 years of evolution, the main changes occur at the head of the estuary, where the tidal distortion starts to promote ebb dominance, acting in the same direction as the subtidal flow. After 200 years, due to the erosion of the upper estuary, the tidal distortion and subtidal flows close to the head reduce intensity and, consequently, sediment transport is smaller.

The cross-channel distribution of the along-channel subtidal sediment transport proxy shows that the main along-channel sediment transport driver is also the subtidal flow (Figure 7). At the beginning of the simulation, in the shallower lateral flanks, the subtidal sediment transport in the middle and lower estuary is toward the ocean and toward the head along the deeper main channel. Because of the morphodynamic feedbacks, the system generates shallower tidal flats and a deeper channel located on the right side (looking into the estuary). After 200 years in the channel (right) the along-channel subtidal sediment transport is toward the inner estuary and at the shallow flats (left) toward the ocean. Throughout the evolution of the estuary, the main driver of the subtidal sediment transport in the middle and lower estuary is the subtidal flow and, specifically, the nonlinear interaction between the subtidal flow and tidal velocities.

3.2. Effects of Density Gradients

To evaluate the effect of density gradient-driven flows on morphological evolution, model runs with uniform density are compared to runs that include salinity gradients. In the baroclinic case described in section 3.1, the main driver of sediment transport is the density-driven flow. Conversely, in the barotropic cases, the main driver of the subtidal sediment transport in the upper estuary is the tidal distortion. The river flow and the tidal distortion generate a subtidal sediment transport convergence in the upper estuary. The morphodynamic evolution of the baroclinic and barotropic simulations is different (Figure 8). In all cases, a sediment transport convergence zone is observed in the upper estuary. In the baroclinic simulations, this convergence is stronger, since both tidal distortion and the baroclinic subtidal flow act in the same direction. In the barotropic simulation the convergence is due to the river flow and the tidal distortion only.

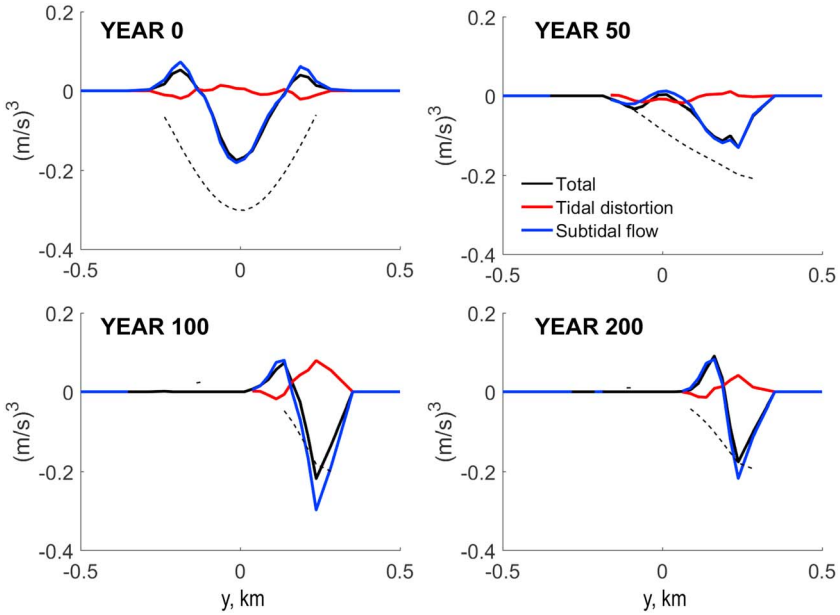

Figure 7. Temporal evolution of along-channel subtidal sediment transport proxies applied to the bottom model cell at a cross-channel section located at x = 80 km. Dashed line indicates shape of the bottom. Positive values indicate sediment transport proxy toward the ocean.

In the barotropic simulation, in the middle and lower estuary, the main driver is the barotropic subtidal flow, which is directed toward the ocean. This creates a subtidal sediment transport divergence in the mid-estuary and a net tendency toward erosion. In the baroclinic simulation, the effects of the barotropic subtidal flows are counteracted by the density-driven circulation, which acts in the opposite direction close to the bottom. In this case, close to the upper estuary the subtidal sediment convergence is enhanced because both subtidal flows near the bottom and tidal distortion act in the same direction. As shown in Figure 8a, the effects of density-driven flows are to accelerate the import of sediment to the upper estuary, to reduce the water

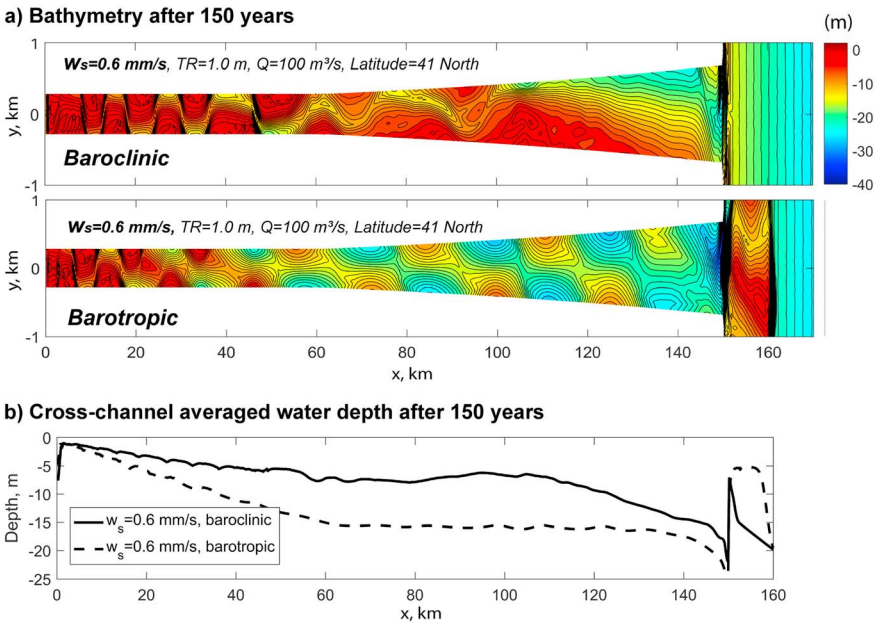

Figure 8. Comparison of the (a) bathymetries and (b) cross-channel averaged water depth after 150 years.

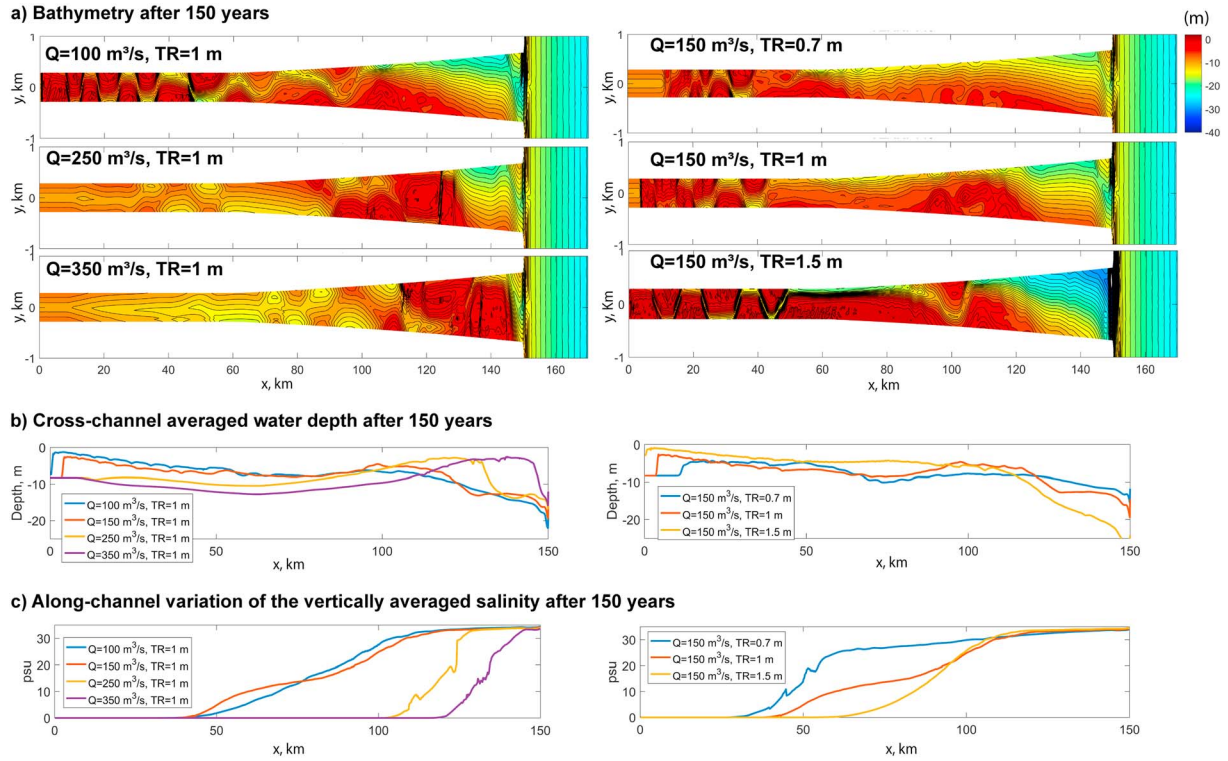

Figure 9. (a) Bathymetry after 150 years of evolution for different river discharge and tidal range, (b) cross-channel averaged bed profile along the estuary, (c) along-channel variation of the vertically averaged salinity after 150 years. (w_s = 0.6 mm/s and latitude = 41°N).

depths in the upper and middle estuary, to promote a faster connection between the meander zone and the middle estuary, to reduce the volume of the ebb-tidal delta, to hamper the formation of alternate bars, and to promote the formation of asymmetric cross-channel bathymetric shapes (in high latitudes due to the combined effect of baroclinicity and Coriolis acceleration as explained in section 3.4). The cross-channel averaged water depth profile along the estuary shows that the concavity of the along-estuary profile is reduced because of the baroclinic effects (Figure 8b).

3.3. Effects of River Discharge and Tidal Range

As the river discharge/velocity increases, in cases which include density gradients, the freshwater-influenced region extends lower into the estuary (Figure 9a). In this river-dominated region, the subtidal velocity is weak, vertically homogeneous, and is directed toward the ocean. At the saltwater intrusion limit there is a subtidal flow convergence zone, where most of the sediment deposition and consequent formation of meanders (characteristic of the tidal-fluvial transition zone) occurs. While in the weak river discharge (100 m^3/s) case the maximum sediment accumulation is observed close to the estuary head (grid boundary), with larger river discharges this accumulation zone moves to the lower estuary (Figure 9b). The increase of the river discharge pushes the salt intrusion limit and, therefore, the whole estuary, toward the ocean (Figure 9c). In this specific estuary, the preimposed width convergence is weak. This implies that changes in river discharge affect a longer distance along the estuary.

The increase of the tidal range produces an increase of the M_2 velocity amplitude, bottom stress, sediment concentration, and the nonlinearity of the system and, consequently, strengthens the subtidal sediment transport. This accelerates the sediment import into the estuary. As the tidal range increases, the elevation of the tidal flats and the maximum water depths along the main channel increase (Figures 9a and 9b). The meanders located at the tidal-fluvial transition zone show a higher wavelength and extend over a larger region (Figure 9c). The salinity intrusion limit is affected by the morphodynamic evolution and reduces as the tidal range increases. This is a consequence of a smaller cross-section averaged water depths and area. Since the strength of the subtidal sediment transport depends on the tidal velocity, the rate of

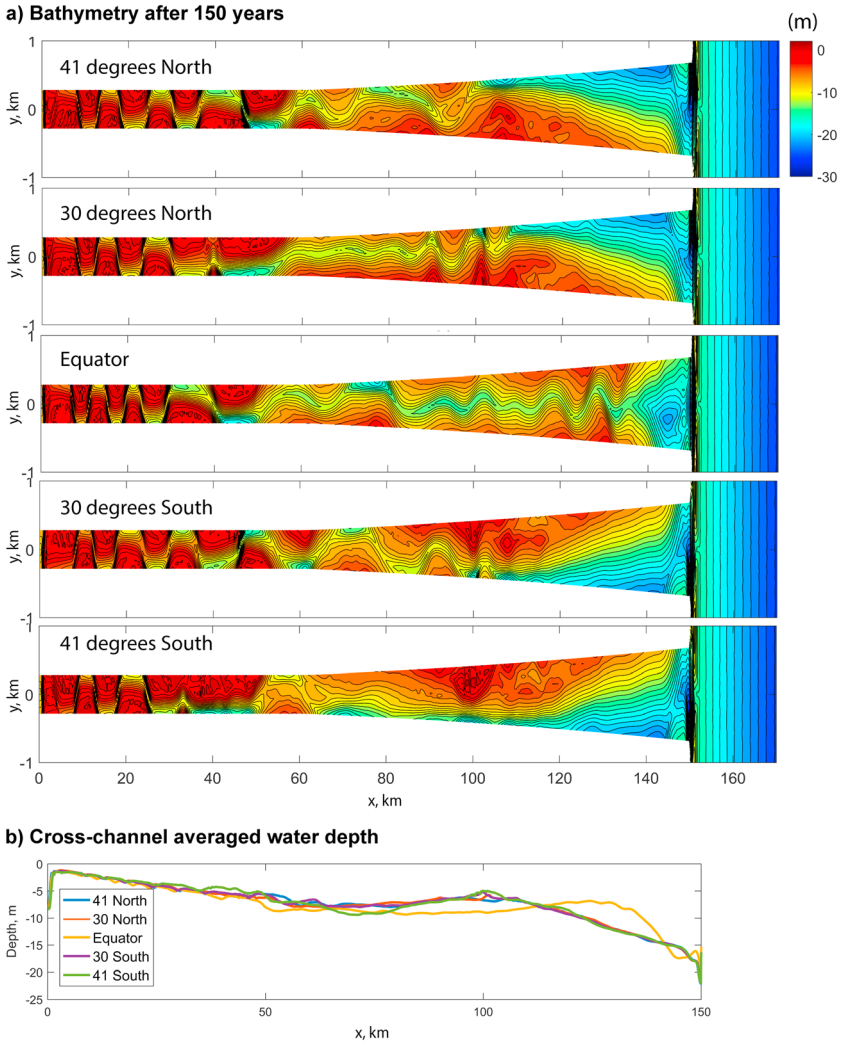

Figure 10. (a) Bathymetries after 150 years and (b) cross-channel averaged bed profile along the estuary for different latitudes. (w_s = 0.6 mm/s, Q = 100 m^3/s, TR = 1 m).

morphological change also varies with tidal range. Some of the variability in morphology for different tidal range is indicative of differences in the evolution timescale rather than representing differences in the equilibrium state of the estuary.

3.4. Effects of Earth's Rotation

One of the notable characteristics of the morphodynamic evolution of these simulations is the development of an asymmetric bathymetry, with the tidal flats in the left and the main channel at the right (looking into the estuary). The degree and sense of the asymmetry depend on the latitude (Figure 10) because of the strength and direction of the Coriolis acceleration. The asymmetry increases with the latitude and is opposite in the Southern Hemisphere. The estuary located at the equator does not show any asymmetry.

The morphologies of estuaries located at same latitudes in the Southern and Northern Hemispheres are not exactly mirrors because of the random perturbations imposed in the initial bathymetry. The cross-channel averaged bed profiles (Figure 10b) for estuaries located at different latitudes or in the Southern and Northern Hemispheres do not show significant changes on the along estuary bed profiles. However, the estuary located at the equator shows a deeper region close to the mouth and shallower depths between x = 120 and 140 km.

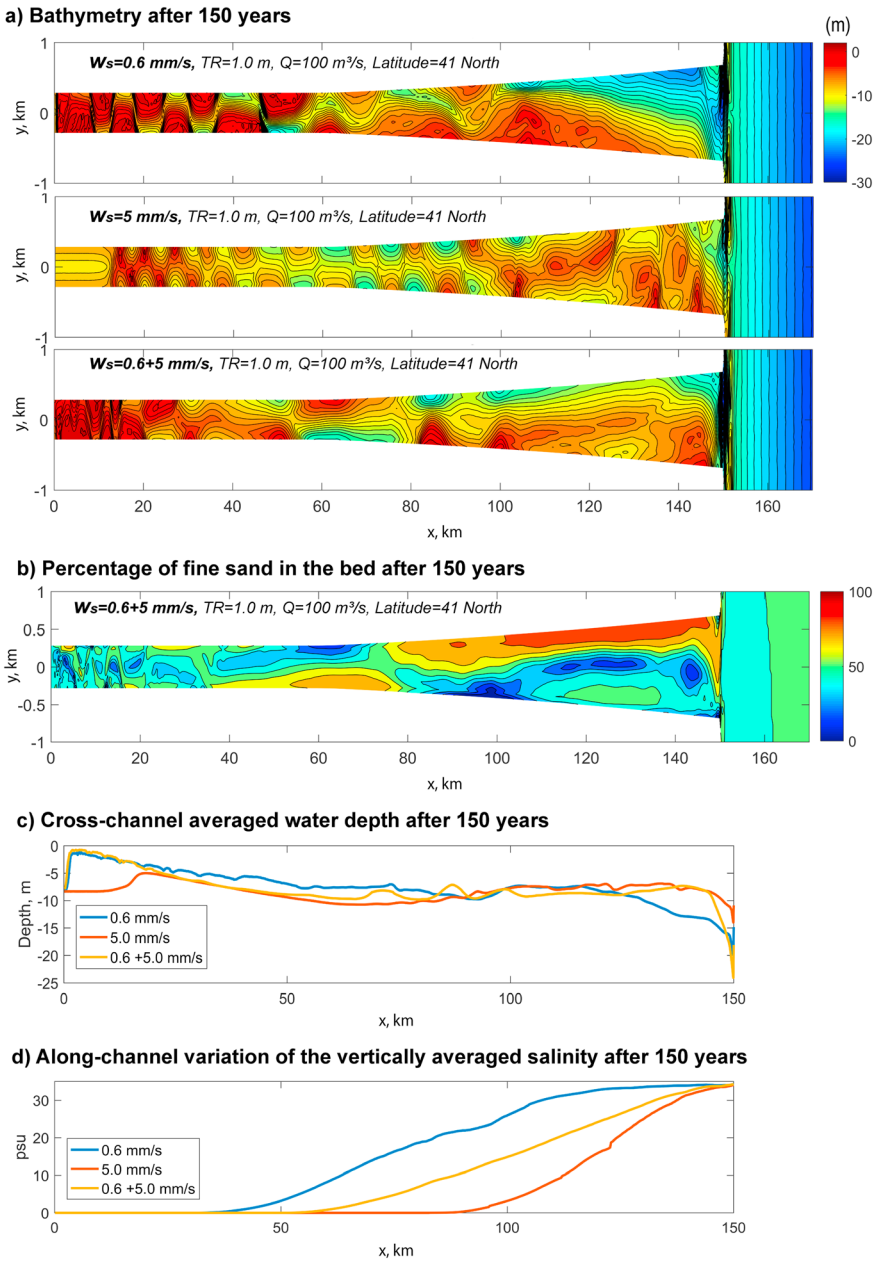

Figure 11. (a) Bathymetries, (b) relative percentage of fine sand, (c) cross-channel averaged bed profile along the estuary, and (d) depth-averaged salinity along the estuary after 150 years for different sediment characteristics. (Q = 100 m^3/s, TR = 1 m, and latitude = 41°N).

The equivalent barotropic simulations did not develop significant asymmetry (not shown). This indicates that the combined effect of baroclinic and Coriolis acceleration is responsible of the development of such asymmetries.

3.5. Effects of Sediment Fall Velocity

Another parameter that affects the morphodynamic evolution is the sediment fall velocity (Figure 11). The coarser the sediment is, the slower the morphodynamic evolution is. Moreover, the capacity of the tidal distortion in the upper estuary to transport sediment and the import to the head diminish. With a fall velocity of 0.6 mm/s, the salinity gradient along the thalweg extends along the whole estuary after 100 years. At the head, the tidal distortion and the subtidal flow transport sediment toward the head, where a meander

system is developed. With a fall velocity of 5 mm/s, the development of the estuary profile is much slower. Close to the, head the initial formation of a bar is observed (at x = 15 km). Oceanward (between x = 15 and 100 km), an alternate bar system is developed. In the lower estuary, water depths after 150 years of evolution are 5 to 10 m shallower than in the fine sediment estuary, and the thalweg is less well developed. The consequent increase of friction and mixing hampers the tidal propagation. The poorly developed thalweg means that salt water does not easily move landward along a deep channel, and this system is more efficient in transporting freshwater into the lower estuary. Consequently, the saltwater intrusion limit is pushed toward the ocean. After 100 years, the salinity gradient along the estuary is larger for the largest fall velocity case.

If we consider a mixture of two sediment classes with fall velocities of 0.6 (medium silt) and 5 mm/s (fine sand), in the upper estuary the sediment accretion increases. In the lower estuary, cross-channel averaged depths are more similar to those observed for the coarsest grain size. However, the thalweg is better developed than in the coarsest case. In this specific case a clear sediment sorting occurs with fine sediment over the flats and the upper estuary region and with a higher fraction of coarser sediment over the main channel and lower estuary (Figure 11b). Initially, fine sand and medium silt fractions are equally distributed (the initial percentage is 50% for each sediment class). Because of the intermediate development of the thalweg, the along-channel salinity gradient after 100 years is higher than the observed for the fine sediment but weaker than the one observed for the coarser sediment (Figure 11d).

3.6. Effects of Baroclinicity in Mesotidal Estuaries

The bathymetric evolution of an idealized higher tide range estuary (3.5-mocean tidal range) also shows the development of an asymmetric channel, with accumulation of sediment in the left side of the estuary and the formation of a main channel on the right side (in the Northern Hemisphere), when the salinity variations are accounted for (Figure 12). In this simulation, two different noncohesive sediment classes, with fall velocities equal to 0.6 and 5 mm/s, have been considered. The tidal asymmetry at the head of the estuary is higher than in the microtidal cases, and both in the baroclinic and in the barotropic simulations, the degree of development of the fluvial-tidal transition zone is similar after 150 years. In the baroclinic case, the meanders of this zone are not as clear as in the barotropic case because of the strong cross-channel bathymetric asymmetry. The bathymetry of the Gironde estuary (mouth tidal range 1.3 m at neap and 5 m at spring; Sottolichio et al., 2013) is shown for comparison in Figure 12d. Like the baroclinic simulation, it exhibits an asymmetrical channel, with the deeper main channel to the left (when looking seaward).

4. Discussion

4.1. Similarities With Real Estuaries

As explained by Dalrymple et al. (2012), tide-dominated estuaries can be divided in two main morphological zones, based on the nature of the channel networks:

1. The outer estuary with several ebb- and flood-dominated channels that separate elongated tidal bars and/or sand flats.
2. A narrower inner estuary that is characterized by a single main ebb-channel bordered by muddy tidal flats and salt marshes.

Many funnel-shaped estuaries are hypersynchronous (Dyer, 1997; Nichols & Biggs, 1985; Salomon & Allen, 1983), which means that the tidal amplitude increases landward due to the tidal energy convergence, reaching a maximum value somewhere landward of the coast. Landward this point, due to the reduction of the water depths, bottom friction becomes dominant over the convergence effect, and a tidal amplitude reduction is observed. The longitudinal variation in the peak tidal current speeds mimics the distribution of the tidal range, increasing landward to some maximum value before decreasing to zero at the tidal limit. Dalrymple and Choi (2007) referred to this zone as the tidal maximum zone. The numerical simulations presented in this study show a tendency to create such tidal maximum zone, although the estuary considered here is not long enough to dissipate the tidal signal through the river-dominated region.

Dalrymple et al. (2012) state that density-driven circulation is weak in tide-dominated estuaries and has little or no influence on the transport of bed material. These three-dimensional model results show that the density-driven circulation does matter to along-channel sediment transport in tidally energetic, partially

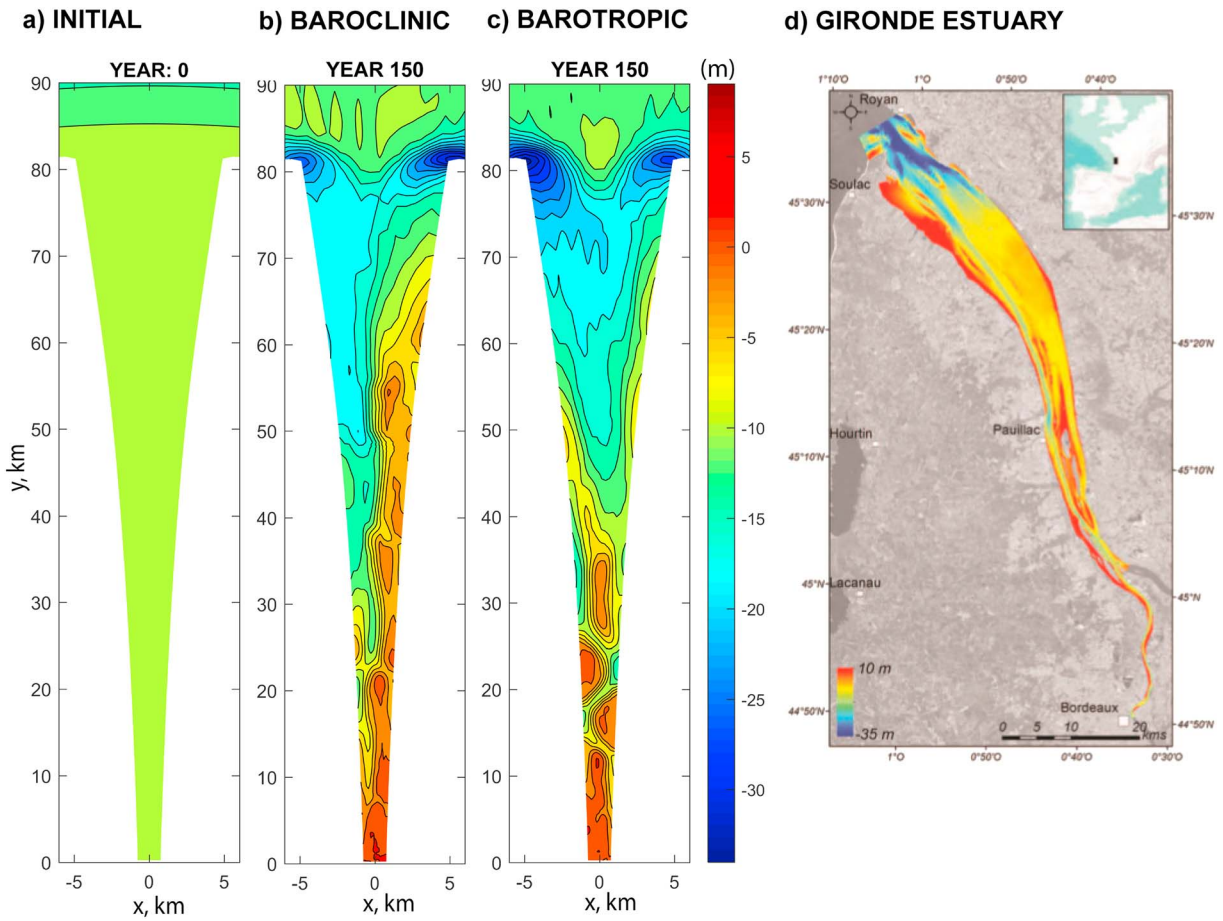

Figure 12. (a) Initial idealized bathymetry of the high tide range idealized estuary, located at a latitude of 45°N, and its modeled bathymetry after 150 years; (b) baroclinic simulations; (c) barotropic simulation; and (d) bathymetry of the Gironde estuary taken from Sottolichio et al., 2013. The simulations are forced with a constant 1.75-m amplitude M_2 tidal wave in the north and a river discharge of 300 m^3/s in the south. Both simulations consider two homogeneously distributed sediment classes with fall velocities of 0.6 and 5 mm/s.

mixed estuaries. Although it is 1 order of magnitude weaker than the M_2 component of tidal velocity, what drives the morphodynamic evolution is the tide-averaged sediment transport. This arises in part from tidal nonlinearity (or tidal distortion) and from the interaction between the tidal flow and the subtidal flow. Net sediment transport due to the latter is proportional to the product of the square of the tidal velocity amplitude and the magnitude of the subtidal flow. This interaction term is, consequently, dependent on both the strength of the tidal currents and subtidal flows. In some conditions, and especially for small *a*/*h* (relative tidal amplitude) values, the tidal-baroclinic interaction term is more important to sediment transport than the tidal distortion itself. This study has shown that subtidal currents driven by density gradient flows are relevant and can play a first-order role on morphodynamics.

The morphological evolution of the idealized transgressive (sediment importing) estuaries considered in this study shows features that are common to real estuaries: in the initial phase of the evolution the head of the estuary accumulates sediment, producing a bar that evolves into a meander system. While alternate bars emerge in the lower and middle estuary during the early phases of the morphodynamic evolution, the cross-channel averaged water depth does not change considerably. During this stage, subtidal flows and tidal distortion produce sediment transport toward the head, and hence, the cross-sectional area and the water depth decrease. The variation of the cross-sectional area and shape of the upper estuary region has two important consequences: (1) the river velocity increases and (2) the tide becomes ebb dominant because of the increase of the intertidal area. Once the meanders are fully developed, the head of the estuary becomes ebb dominant (subtidal flows and tidal distortion produce a net transport toward the lower estuary). The oceanward limit of the meander zone is given by the maximum salinity intrusion, which defines

the Dalrymple et al. (2012) *bed load convergence* zone. It is in this area where the estuarine turbidity maximum is observed. The shallow water depths, high tidal velocities, and the convergence of vertically uniform freshwater velocities and baroclinic flows are the factors that promote high rates of sediment resuspension and retention in the ETM. The reader is referred to Burchard et al. (2018) for a detail description of sediment trapping mechanisms at the salt intrusion limit.

The model is able to reproduce qualitatively some features observed in real estuaries. Microtidal real estuaries with similar tendency to idealized estuaries of this study include the Hudson, James, and the York River estuaries, systems for which conceptual models have hypothesized that asymmetries in bed stress and/or turbulence due to the superposition of tidal and density-driven hydrodynamics suspend and transport more fine sediment on flood, thus leading to net landward transport (Friedrichs, 2009; Geyer et al., 2001; Nichols et al., 1991). Furthermore, in all three of these estuaries, the morphology shows a clear cross-channel asymmetry with the main channel located on the right and the lateral shoals concentrated on the left side when looking into the estuary. Subtidal flow and residual sediment transport patterns also show similar characteristics, with a main inflow in the main channel and an oceanward directed flow over the flanking shallows. For example, the tendency of the model is to create a horizontally sheared subtidal sediment transport structure: subtidal sediment flux is toward the head along the deeper channel, whereas net flux over the lateral shoals/tidal flats is toward the ocean. When considering two sediment classes, there is a clear sediment sorting, with a higher fraction of coarse sediment along the deeper areas and accumulation of fines in the tidal flats, as described for tide-dominated estuaries by Dalrymple et al. (2012). In the lower Hudson River the subtidal sediment transport is seaward over the shoals and toward the head along the main channel (Panuzio, 1965; Ralston et al., 2012). This behavior has also been observed in the York River (Scully & Friedrichs, 2007). In the estuaries such as the Hudson River, baroclinicity enhances the flood dominance and the capacity to import sediment to the estuary.

The effect of subtidal flows on the net sediment transport increases with the enhancement of the subtidal flow magnitude and also with the amplitude of the main astronomic components. The implication is that this effect might be relevant in diverse types of estuaries, and especially in most partially mixed and many well-mixed estuaries, including cases with residual flows driven by eddy viscosity-shear covariance (Dijkstra et al., 2017). In fact, subtidal landward sediment transport driven by the density gradient-induced circulation has been identified in mesotidal partially mixed estuaries (e.g., Carquinez Strait of San Francisco; Ganju & Schoellhamer, 2006). Macrotidal estuaries where the baroclinic influence, and specifically the combined effect of Coriolis and baroclinic forces, might be relevant producing a cross-channel bathymetric asymmetry include the Gironde Estuary (France). The high mesotidal range idealized estuary shown in Figure 12 is representative of estuaries similar to the Gironde estuary (France). Numerical results have shown that, in fact, in these types of estuaries the combined effect of baroclinity and Coriolis acceleration is a main contributor to the morphodynamic evolution.

4.2. Cross-Section Asymmetry

Previous studies (e.g., Hujits et al., 2006, 2009) indicate that the cross-channel bathymetric asymmetry might arise due to the Ekman transport or due to the secondary flow induced by the cross-channel baroclinic gradients. In these studies Coriolis deflection and the secondary flow due to cross-channel density variations are independent and act in opposite ways: while the Coriolis deflection produces a net sediment accumulation on the right side of the estuary (looking up-estuary in the Northern Hemisphere), baroclinicity induces sediment accumulation on the left side. Prior research (e.g., Scully et al., 2009) and our numerical simulations agree that cross-channel density gradients are dependent on the Coriolis acceleration; we have shown that these density gradients are highly dependent on the bathymetry itself.

The morphodynamic simulations shown in this study indicate that indeed, the lateral asymmetry of the along-channel flow and the lateral circulations, induced by the joint effects of Coriolis acceleration and density gradients, leads to asymmetric morphological evolution. In the Northern Hemisphere, the deep channel develops on the right side of the estuary; shallow flanks are observed on the left. The contrary occurs in the Southern Hemisphere, and in the equator no asymmetry is obtained. In our simulations the cross-channel bathymetric asymmetry is initiated by an asymmetry of the along-channel subtidal sediment transport. This asymmetry arises from the nonlinear interaction between the subtidal flow and tidal velocities. The main source of the asymmetry is due to the subtidal flow (Figure 13, top row). The feedback mechanism that

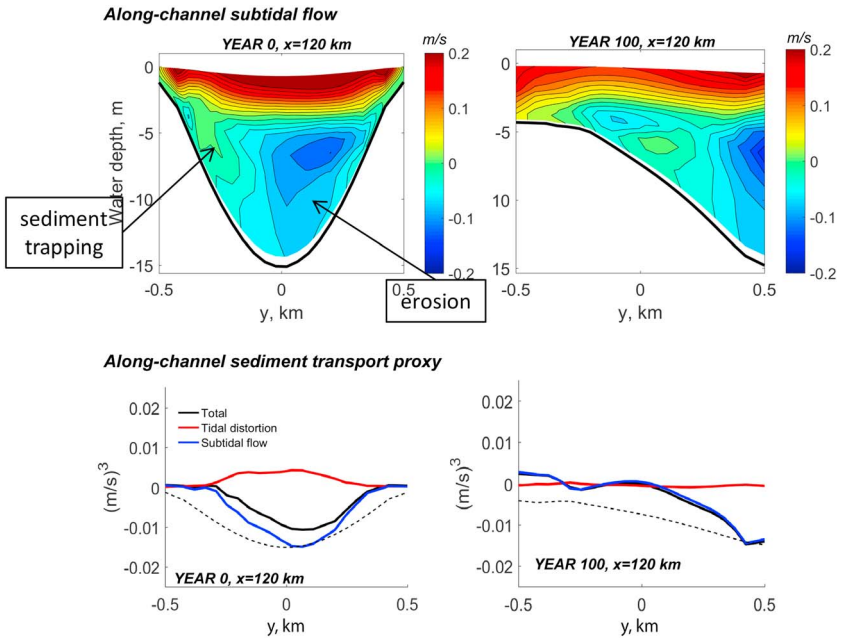

Figure 13. Schematic diagram of the main mechanisms and feedbacks that lead to an asymmetric bathymetry. (top panel) Cross-channel distribution of the along-channel subtidal flow at x = 120 km in years 0 and 100. (bottom panel) Cross-channel distribution of the subtidal sediment transport proxy at x = 120 in years 0 and 100. Dashed line indicates shape of the bottom. Positive sediment transport proxy is directed toward the ocean. Results correspond to the case with Q = 100 m^3/s, TR = 0.7 m, w_s = 0.6 mm/s, latitude = 41°N. In this case, the initial formation of the alternate bars is not as intense as in the simulations with higher tidal amplitudes and it is, therefore, the case in which this positive feedback is the clearest.

causes the asymmetry is schematized in Figure 13 and described below: Initially, in the Northern Hemisphere, because of the lateral advection induced by the combined effect of baroclinicity and Coriolis acceleration, the subtidal flow is asymmetric, with stronger flows toward the head on the right (e.g., Scully et al., 2009). The nonlinear interaction between the laterally sheared subtidal flow and tidal currents results in an asymmetric along-channel sediment transport (Figure 13, bottom row). The right side of the main channel erodes more than the left side, which produces an initial asymmetry of the bathymetry. Because shallow areas are relatively more frictional, the tidal flow reduces in the left and increases in the main channel. This enhances even more the along-channel sediment transport in the main channel relative to the shallower flats located in the left. The cross-channel salinity gradients become larger, especially during the flood, and the lateral advection (Lerczak & Geyer, 2004; Scully et al., 2009) becomes stronger. The secondary flow, directed to the left close to the bottom, and the estuarine circulation intensify, increasing even more the erosion of the main channel and the sediment accretion over the left flats. This enhances even more the mixing and frictional difference induced by the bathymetric changes (e.g., Ralston et al., 2012; Valle-Levinson et al., 2003; Wong, 1994).

As the result of the positive feedbacks between the along-channel and cross-channel sediment transport processes and the bathymetric evolution, the cross-channel bathymetric asymmetry grows until the reduction of the sediment transport capacity in the main channel, due to the deepening, produces a negative feedback. In these numerical simulations, to initiate the positive feedback that leads to the bathymetric asymmetry, it is necessary to have an initially asymmetric cross-channel shear in the along-channel subtidal flow (which results from the combined effect of the density gradient-induced flows and the Coriolis acceleration). In the analyzed barotropic cases, the Coriolis acceleration is not strong enough to initiate and maintain the cross-channel asymmetry.

4.3. Comparison With Previous Studies and Advances and Limitations of the Present Approach

Often, the long-term evolution of estuaries is analyzed using process-based models, which do not consider the effects of salinity or density variations and use a vertically averaged flow and sediment transport

model. In significantly baroclinic estuaries with fine sediment or a mixture of sediments, this approach is not valid as demonstrated in this study. Previous modeling studies with depth-averaged models, in which the Engelund and Hansen (1967) formula is adopted to represent the total sediment transport (e.g., Canestrelli et al., 2014; Van der Wegen et al., 2008), show a net tendency of estuaries to erode. This may in part be because depth-averaged models cannot produce the two-layered, density-driven flows that characteristically drive the import of sediment into estuaries from the sea. In partially and well-mixed estuaries, density-driven residual flows tend to be strongest near the estuary mouth, where depths are greatest. In contrast, flood-dominated barotropic tidal distortion, which is well represented within estuaries by depth-averaged models, is least important at the estuary mouth if oceanic tidal elevation is undistorted. In fact, barotropic tidal currents forced by an undistorted ocean tide tend to be ebb dominant at the estuary mouth due to a partially progressive relationship between tidal elevation and tidal volume flux (Friedrichs et al., 1992). Taken together, these tendencies suggest that depth-averaged models are likely to significantly underestimate the import of marine sediment into estuaries.

Due to the many simplifications considered in this study (e.g., idealized accommodation space and shape of the estuary, constant external forces, no human intervention effects, uniform sediment distribution, and no consolidation effects), it is not feasible to perform a quantitative comparison with the sediment concentration fields or bathymetry of real estuaries. In particular, the assumption of a spatially uniform bed erodibility tends to spread out the estuarine turbidity maximum along channel and overestimate the ETM's correlation to spatial variations in tidal velocity. In reality, erodibility and concentrations in estuaries like the Hudson and York are observed to be highest in narrower turbidity maxima where fine sediments have most recently been deposited (Dickhudt et al., 2009; Ralston et al., 2012).

Another limitation of the model is the preimposed funnel shape and accommodation space of the estuary. In nature, the formation of the funnel shape is a consequence of morphodynamic feedbacks. Since ROMS does not include lateral bank erosion capabilities, we do not think that the funnel shape of the estuary can be correctly reproduced. However, as shown in the manuscript, the model is able to reproduce the cross-sectional area reduction that results from the tidal flux decrease. The lateral constraint should not affect the relationship between cross-sectional area and tidal flux. Although the initial funnel-shape imposition might constrain the formation of long meanders in the region where we observe a relatively straight channel, this imposition should not affect the validity of one of our main points: from a higher sinuosity region that characterizes the fluvial-tidal transition zone, baroclinicity reduces the degree of meandering or sinuosity in the zone affected by the salinity gradients. The reduction of the meandering degree in the salinity gradient affected region has been observationally documented by several authors (Dalrymple et al. 1992, 2012; Nichols et al., 1991).

The present model is able to reproduce many morphodynamic features observed in real estuaries indicating that the model's overall tendency is similar to the tendency observed in nature. However, the simulated morphodynamic evolution seems to be faster than what is observed in nature. In the numerical simulations with highest tidal ranges, after 200 years, the simulated system starts to transition into a prograding system. In estuaries such as the York or Hudson Rivers this transition has not happened yet, which suggests that such transitions usually take longer periods. These higher evolution rates observed in the simulations are expected since we are disregarding consolidation effects, and we are forcing the system with constant tides and river fluxes. If erodibility of fine sediment were allowed to increase at locations of recent deposition, increased local resuspension and a stronger resulting settling lag effect would drive some sediment away from the depocenters, slowing morphological change (Friedrichs et al., 1998). And if natural discharge cycles were included, some of the sediment previously trapped in the estuary might be seasonally flushed from the system (Ralston & Geyer, 2009). We are also not including the effect of wind and wind waves, which might erode the tidal flats. Effects of vegetation, sediment flocculation, and bioturbation have likewise been disregarded. Since most of these biological/ecological processes depend on the salinity distribution along the estuary, we believe that biologically affected morphodynamic feedbacks should also take into consideration the evolution of the salinity field, which is highly dependent on the morphology.

More importantly, in this study we are not simulating the evolution of the estuaries from their genesis to the present situation. For that we would have to simulate the sea level rise during the last postglacial era and the creation of accommodation space due to the flooding of river mouth areas. These areas were not initially filled with sediments, and the sediment import from the river and the sea occurred during a much longer

period. Conversely, in this study we assumed that the sediment is already in the estuary or available in the ocean side (no sediment inputs are considered from the river boundary), and what we simulate is how this sediment is redistributed within the estuary as a response to the external forces. This might appear a coarse approach to the problem, but the fact that the model has the tendency to reproduce some key features observed in real estuaries is encouraging. Our goal with this study is not to get the rate of evolution of estuaries, which is extremely challenging due to all the aforementioned reasons. The main goal is to obtain a morphodynamic evolution tendency observed in baroclinic estuaries characterized by fine sediments and understand the possible feedback mechanisms arising because of the density-driven and three-dimensional subtidal circulation, customary to many diverse estuaries around the world.

This study also poses some new challenges to the physical modeling techniques used to analyze the morphodynamic evolution of estuaries. Physical models usually do not consider the effect of baroclinicity, and they are not able to import sediments due to density-driven flows. Moreover, given the reduced scale of these models, the effect of the Earth's rotation is difficult to simulate, and the combined effect of baroclinity and Coriolis might be extremely challenging to account for. Nonetheless, the current study and the similarities observed between estuaries such as Gironde, York, James, and Hudson estuaries concerning the asymmetric cross-channel bathymetry suggest that this combined effect is a leading mechanism driving the morphodynamic evolution of estuaries.

5. Summary and Conclusions

The COAWST modeling system is applied in an idealized, muddy, funnel-shaped estuary to analyze the effects of density-driven flows in their long-term morphodynamic evolution. Three-dimensionality, density variations, and the Earth's rotation are all found to be essential ingredients of the morphodynamic evolution. These barotropic simulations reproduce the alternate bar systems observed in previous studies (e.g., Hibma et al., 2004; Van der Wegen et al., 2008). In these simulations, tidal distortion tends to accumulate sediment in the upper estuary and barotropic subtidal flows tend to erode the middle and lower zones. The overall behavior of the barotropic simulations is erosional. Conversely, the baroclinic simulations show an overall accretive tendency induced by the three-dimensional circulation. Density gradient-driven flows have leading order effects of the morphodynamic evolution. The main effects are (1) to promote near-bed flood dominance and therefore the import of sediment into the estuary, (2) to accelerate the morphodynamic evolution of the upper/middle estuary, (3) to produce a more concave shape of the upper estuary and reduction of the ebb-tidal delta volume, and (4) via the combined effect of Earth's rotation and baroclinicity, to produce an asymmetric bathymetry and hamper the production of alternate bars that form under barotropic conditions.

Results with different river discharges have shown that for a fixed tidal range, an increase in the river discharge displaces oceanward the region where density gradients are relevant and displaces the meandering zone lower into the estuary. The increase of the tidal range and, therefore, sediment concentration and the nonlinearity of the system enhances the magnitude of the subtidal sediment transport, which accelerates the morphodynamic evolution. The increase of the tidal range reduces the water depth of the lateral shoals/flats via deposition, increases the accretion in the upper estuary, and increases the maximum water depths along the main channel. Estuaries located at different latitudes might also show different morphologies, since the combined effect of baroclinicity and Coriolis tends to produce an asymmetry of the bathymetry and flow in the cross-channel direction. In the Northern Hemisphere this results in the development of a deep channel on the right side of the estuary and shoals/flats on the left (looking into the estuary). The opposite tendency is observed in the Southern Hemisphere, and no apparent asymmetry is obtained at the equator. This asymmetry, induced by the combined effect of Coriolis acceleration and density-driven flows, requires an initial asymmetric cross-channel shear in the along-channel subtidal flow. This produces a higher erosion on one side of the estuary, and due to the lateral advection effect (Lerczak & Geyer, 2004; Scully et al., 2009) and bathymetric effects on the flow (Valle-Levinson et al., 2003), the subtidal sediment transport becomes even more asymmetric.

We have applied the morphodynamic model in a high mesotidal range estuary that resembles the estuarine parameter space characteristic of the Gironde estuary, to show that this feedback mechanism is relevant in estuaries with higher tidal ranges. Modeled bathymetries resemble the main structure of the Gironde Estuary, in which the main channel is located on the right side and the fine sediment flats are on the left.

Nonetheless, we have neglected many processes that might play a critical role on the morphodynamic evolution of estuaries.

Further research is needed to address the implications of changing forcing conditions in the current climate change scenario. It is important to consider that the effect of the sea level rise might be relevant for the future evolution of our estuaries; however, as suggested by the present study, changes in the freshwater discharge might also play a critical role in such evolution.

An important take home message of the present study is that we should not a priori neglect the effects of baroclinicity and Coriolis even in mesotidal to macrotidal estuaries. Subtidal flows play a critical role in the morphodynamic evolution. Bathymetric control in these types of coastal systems is as relevant as the hydrodynamics, and each is mutually dependent on each other.

Acknowledgments
We are grateful to all the developers of the COAWST, ROMS, and CSTMS modeling systems. M. O. acknowledges support from NSF project OCE-1554892. W. R. G. acknowledges support from NFS project OCE-1634480. C. T. F. acknowledges support from NSF project OCE-1459708. Z. C. acknowledges the University of Florida for supporting his PhD, through a Graduate Fellow Scholarship. COAWST is an open source code and can be downloaded as explained in the following website: https://woodshole.er.usgs.gov/operations/modeling/COAWST. Model results and scripts to create the figures are accessible in the Figshare repository (DOI: 10.6084/m9.figshare.5975164).

References

Bagnold, R. A. (1966). An approach to the sediment transport problem from general physics. *Geological Survey Professional paper 422-1*. Washington, DC: US Government Printing Office.

Burchard, H., Schuttelaars, H. M., & Ralston, D. K. (2018). Sediment trapping in estuaries. *Annual Review of Marine Science*, *10*(1), 371–395. https://doi.org/10.1146/annurev-marine-010816-060535

Canestrelli, A., Lanzoni, S., & Fagherazzi, S. (2014). One-dimensional numerical modeling of the long-term morphodynamic evolution of a tidally-dominated estuary: The lower Fly River (Papua New Guinea). *Sedimentary Geology*, *301*, 107–119. https://doi.org/10.1016/j.sedgeo.2013.06.009

Chassignet, E. P., Arango, H., Dietrich, D., Ezer, T., Ghil, M., Haidvogel, D. B., et al. (2000). DAMEE-NAB: The base experiments. *Dynamics of Atmospheres and Oceans*, *32*(3-4), 155–183. https://doi.org/10.1016/S0377-0265(00)00046-4

Chernetsky, A. S., Schuttelaars, H. M., & Talke, S. A. (2010). The effect of tidal asymmetry and temporal settling lag on sediment trapping in tidal estuaries. *Ocean Dynamics*, *60*(5), 1219–1241. https://doi.org/10.1007/s10236-010-0329-8

Coco, G., Zhou, Z., van Maanen, B., Olabarrieta, M., Tinoco, R., & Townend, I. (2013). Morphodynamics of tidal networks: Advances and challenges. *Marine Geology*, *346*, 1–16. https://doi.org/10.1016/j.margeo.2013.08.005

Dalrymple, R. W. (2006). Incised valleys in time and space: Introduction to the volume and an examination of the controls on valley formation and filling. In R. W. Dalrymple, D. A. Leckie, & R. Tillman (Eds.), *Incised valleys in time and space*, *SEPM Special publication*, (Vol. 85, pp. 5–12).

Dalrymple, R. W., & Choi, K. S. (2007). Morphologic and facies trends through the fluvial-marine transition in tide-dominated depositional systems: A systematic framework for environmental and sequence-stratigraphic interpretation. *Earth-Science Reviews*, *81*(3-4), 135–174. https://doi.org/10.1016/j.earscirev.2006.10.002

Dalrymple, R. W., Mackay, D. A., Ichaso, A. A., & Choi, K. S. (2012). Processes, morphodynamics, and facies of tide-dominated estuaries. In R. A. Davis, & R. W. Dalrymple (Eds.), *Principles of tidal sedimentology*. Dordrecht Heidelberg London New York: Springer.

Dalrymple, R. W., Zaitlin, B., & Ron, B. R. (1992). Estuarine facies models: conceptual basis and stratigraphic implications. *Journal of Sedimentary Research*, *62*(6), 1130–1146. https://doi.org/10.1306/D4267A69-2B26-11D7-8648000102C1865D

De Swart, H. E., & Zimmerman, J. T. F. (2009). Morphodynamics of tidal inlet systems. *Annual Review of Fluid Mechanics*, *41*(1), 203–229. https://doi.org/10.1146/annurev.fluid.010908.165159

Dickhudt, P. J., Friedrichs, C. T., Schaffner, L. C., & Sanford, L. P. (2009). Spatial and temporal variation in cohesive sediment erodibility in the York River estuary, eastern USA: A biologically influenced equilibrium modified by seasonal deposition. *Marine Geology*, *267*(3-4), 128–140. https://doi.org/10.1016/j.margeo.2009.09.009

Dijkstra, Y. M., Brouwer, R. L., Schuttelaars, H. M., & Schramkowski, G. P. (2017). The iFlow modelling framework v2. 4: A modular idealized process-based model for flow and transport in estuaries. *Geoscientific Model Development*, *10*(7), 2691–2713. https://doi.org/10.5194/gmd-10-2691-2017

Dijkstra, Y. M., Schuttelaars, H. M., & Burchard, H. (2017). Generation of exchange flows in estuaries by tidal and gravitational eddy viscosity-shear covariance (ESCO). *Journal of Geophysical Research: Oceans*, *122*, 4217–4237. https://doi.org/10.1002/2016JC012379

Dronkers, J. (2017). Convergence of estuarine channels. *Continental Shelf Research*, *144*, 120–133. https://doi.org/10.1016/j.csr.2017.06.012

Dyer, K. R. (1995). Sediment transport processes in estuaries. In G. M. E. Perillo (Ed.), *Geomorphology and sedimentology of estuaries. Development in sedimentology*, (Vol. 53, pp. 423–449). Amsterdam: Elsevier. https://doi.org/10.1016/S0070-4571(05)80034-2

Dyer, K. R. (1997). *Estuaries—A physical introduction*, (2nd ed.). New York: Wiley. 195 p

Engelund, F., & Hansen, E. (1967). *A Monograph on sediment transport in alluvial streams*. Copenhagen, Denmark: Teknisk Forlag.

Fagherazzi, S., & Furbish, D. J. (2001). On the shape and widening of salt marsh creeks. *Journal of Geophysical Research*, *106*(C1), 991–1003. https://doi.org/10.1029/1999JC000115

Fortunato, A. B., & Oliveira, A. (2005). Influence of intertidal flats on tidal asymmetry. *Journal of Coastal Research*, *215*, 1062–1067. https://doi.org/10.2112/03-0089.1

Fortunato, A. B., Oliveira, A., & Baptista, A. M. (1999). On the effect of tidal flats on the hydrodynamics of the Tagus estuary. *Oceanologica Acta*, *22*(1), 31–44. https://doi.org/10.1016/S0399-1784(99)80030-9

Friedrichs, C. T. (2009). York River physical oceanography and sediment transport. *Journal of Coastal Research*, *57*, 17–22.

Friedrichs, C. T., Armbrust, B. D., & de Swart, H. E. (1998). Hydrodynamics and equilibrium sediment dynamics of shallow, funnel-shaped tidal estuaries. In J. Dronkers & M. B. A. M. Scheffers (Eds.), *Physics of Estuaries and Coastal Seas* (pp. 315–327). Brookfield, Vt: A. A. Balkema.

Friedrichs, C. T., & Aubrey, D. G. (1988). Non-linear tidal distortion in shallow well-mixed estuaries: A synthesis. *Estuarine, Coastal and Shelf Science*, *27*, 521–545.

Friedrichs, C. T., Lynch, D. R., & Aubrey, D. G. (1992). Velocity asymmetries in frictionally-dominated tidal embayments. *Dynamics and Exchanges in Estuaries and the Coastal Zone*, 277–312. https://doi.org/10.1029/CE040p0277

Ganju, N., Schoellhamer, D., & Jaffe, B. E. (2009). Hindcasting of decadal-timescale estuarine bathymetric change with a tidal-timescale model. *Journal of Geophysical Research*, *114*, F04019. https://doi.org/10.1029/2008JF001191

Ganju, N. K., & Schoellhamer, D. H. (2006). Annual sediment flux estimates in a tidal strait using surrogate measurements. *Estuarine, Coastal and Shelf Science*, *69*(1-2), 165–178. https://doi.org/10.1016/j.ecss.2006.04.008

Geyer, W. R., & MacCready, P. (2014). The estuarine circulation. *Annual Review of Fluid Mechanics*, *46*(1), 175–197. https://doi.org/10.1146/annurev-fluid-010313-141302

Geyer, W. R., Woodruff, J. D., & Traykovski, P. (2001). Sediment transport and trapping in the Hudson River estuary. *Estuaries and Coasts*, *24*(5), 670–679. https://doi.org/10.2307/1352875

Gräwe, U., Burchard, H., Müller, M., & Schuttelaars, H. M. (2014). Seasonal variability in M2 and M4 tidal constituents and its implications for the coastal residual sediment transport. *Geophysical Research Letters*, *41*, 5563–5570. https://doi.org/10.1002/2014GL060517

Guo, L., van der Wegen, M., Roelvink, J. A., & He, Q. (2014). The role of river flow and tidal asymmetry on 1-D estuarine morphodynamics. *Journal of Geophysical Research: Earth Surface*, *119*, 2315–2334. https://doi.org/10.1002/2014JF003110

Haidvogel, D. B., Arango, H., Budgell, W. P., Cornuelle, B. D., Curchitser, E., Di Lorenzo, E., et al. (2008). Ocean forecasting in terrain-following coordinates: Formulation and skill assessment of the Regional Ocean Modeling System. *Journal of Computational Physics*, *227*(7), 3595–3624. https://doi.org/10.1016/j.jcp.2007.06.016

Haidvogel, D. B., Arango, H. G., Hedstrom, K., Beckmann, A., Malanotte-Rizzoli, P., & Shchepetkin, A. F. (2000). Model evaluation experiments in the North Atlantic Basin: Simulations in nonlinear terrain-following coordinates. *Dynamics of Atmospheres and Oceans*, *32*(3-4), 239–281. https://doi.org/10.1016/S0377-0265(00)00049-X

Hibma, A., de Vriend, H. J., & Stive, M. J. F. (2003a). Numerical modeling of shoal pattern formation in well-mixed elongated estuaries. *Estuarine, Coastal and Shelf Science*, *57*(5-6), 981–991. https://doi.org/10.1016/S0272-7714(03)00004-0

Hibma, A., Schuttelaars, H. M., & Wang, Z. B. (2003b). Comparison of longitudinal equilibrium profiles of estuaries in idealized and process-based models. *Ocean Dynamics*, *53*(3), 252–269. https://doi.org/10.1007/s10236-003-0046-7

Hibma, A., Stive, M. J. F., & Wang, Z. B. (2004). Estuarine morphodynamics. *Coastal Engineering*, *8–9*, 765–778.

Huijts K. M. H., Schuttelaars H. M., De Swart H. E., Friedrichs C. T. (2009). Analytical study of the transverse distribution of along-channel and transverse residual flows in tidal estuaries. *Continental Shelf Research*, *29*, 89–100.

Huijts K. M. H., Schuttelaars H. M., De Swart H. E., & Valle-Levinson A. (2006). Lateral trapping of sediment in tidal estuaries: An idealized model. *Journal of Geophysical Research*, *111*, C12016. https://doi.org/10.1029/2006JC003615

Huijts K. M. H., De Swart H. E., Schramkowski G. P., & Schuttelaars H. M.. (2011). Transverse structure of tidal and residual flow and sediment concentration in estuaries. *Ocean Dynamics*, *61*, 8, 1067–1091. https://doi.org/10.1007/s10236-011-0414-7

Iwasaki, T., Shimizu, Y., & Kimura, I. (2013). Modelling of the initiation and development of tidal creek networks. Proceedings of the ICE. *Maritime Engineering*, *166*(2), 76–88. https://doi.org/10.1680/maen.2012.12.

Kennish, M. J. (2002). Environmental threats and environmental future of estuaries. *Environmental Conservation*, *29*(1), 78–107.

Kleinhans, M., Van der Vegt, M., Van Scheltinga, R., Baar, A., & Markies, H. (2012). Turning the tide: Experimental creation of tidal channel networks and ebb deltas. *Netherlands Journal of Geosciences*, *91* (3), 311–323.

Lanzoni, S., & Seminara, G. (2002). Long-term evolution and morphodynamic equilibrium of tidal channels. *Journal of Geophysical Research*, *107*(C1), 3001. https://doi.org/10.1029/2000JC000468

Lerczak, J. A., & Geyer, W. R. (2004). Modeling the lateral circulation in straight, stratified estuaries. *Journal of Physical Oceanography*, *34*(6), 1410–1428. https://doi.org/10.1175/1520-0485(2004)034<1410:MTLCIS>2.0.CO;2

Lesser, G. R., Roelvink, J. A., Van Kester, J. A. T. M., & Stelling, G. S. (2004). Development and validation of a three-dimensional morphological model. *Coastal Engineering*, *51*(8-9), 883–915. https://doi.org/10.1016/j.coastaleng.2004.07.014

MacCready, P., & Geyer, W. R. (2010). Advances in estuarine physics. *Annual Review of Marine Science*, *2*(1), 35–58. https://doi.org/10.1146/annurev-marine-120308-081015

Marciano, R., Wang, Z. B., Hibma, A., de Vriend, H. J., & Defina, A. (2005). Modeling of channel patterns in short tidal basins. *Journal of Geophysical Research*, *110*, F01001. https://doi.org/10.1029/2003JF000092

Myrick, R. M., & Leopold, L. B. (1963). Hydraulic geometry of a small tidal estuary. *U.S. Geological Survey Professional Paper 422-B*, 18 p.

Nichols, M. M., & Biggs, R. B. (1985). Estuaries. In R. A. Davis (Ed.), *Coastal sedimentary environments* (2nd ed. pp. 77–186). New York: Springer. https://doi.org/10.1007/978-1-4612-5078-4_2

Nichols, M. M., Johnson, G. H., & Peebles, P. C. (1991). Modern sediments and facies model for a microtidal coastal plain estuary, the James Estuary, Virginia. *Journal of Sedimentary Research*, *61*(6).

Panuzio, F. L. (1965). Lower Hudson River siltation. In *Proceedings of the 2nd Federal Interagency Sedimentation Conference, Misc. Publ. 970* (pp. 512–550). Washington, DC: Agricultural Research Service, U.S. Department of Agriculture.

Perillo, G. M. E. (Ed.) (1995). *Geomorphology and sedimentology of estuaries, development sedimentology* (Vol. 53). Amsterdam: Elsevier, Science.

Ralston, D. K., & Geyer, W. R. (2009). Episodic and long-term sediment transport capacity in the Hudson River estuary. *Estuaries and Coasts*, *32*(6), 1130–1151. https://doi.org/10.1007/s12237-009-9206-4

Ralston, D. K., Geyer, W. R., & Warner, J. C. (2012). Bathymetric controls on sediment transport in the Hudson River estuary: Lateral asymmetry and frontal trapping. *Journal of Geophysical Research*, *117*, C10013. https://doi.org/10.1029/2012JC008124

Reynolds, O. (1889). Report of the committee appointed to investigate the action of waves and currents on the beds and foreshores of estuaries by means of working models. British Association Report, Technical Report 1.

Reynolds, O. (1890). Second report of the committee appointed to investigate the action of waves and currents on the beds and foreshores of estuaries by means of working models. British Association Report, Technical Report II.

Reynolds, O. (1891). Third report of the committee appointed to investigate the action of waves and currents on the beds and foreshores of estuaries by means of working models. British Association Report, Technical Report III.

Rinaldo, A., Belluco, E., D'Alpaos, A. F., Lanzoni, S., & Marani, M. (2004). Tidal networks: Form and function. In S. Fagherazzi, L. Blum, & M. Marani (Eds.), *Ecogeomorphology of tidal marshes. American Geophysical Union*, *Coastal and Estuarine Monograph Series* (Vol. 59, pp. 75–91). Washington, DC: American Geophysical Union.

Robb, C. K. (2014). Assessing the impact of human activities on British Columbia's estuaries. *PLoS One*, *9*(6), e99578. https://doi.org/10.1371/journal.pone.0099578

Roelvink, J. A. (2006). Coastal morphodynamic evolution techniques. *Coastal Engineering*, *53*(2–3), 277–287. https://doi.org/10.1016/j.coastaleng.2005.10.015

Salomon, J. C., & Allen, G. P. (1983). Role sedimentologique de la mare dans les estuaires a fort marnage. *Compagnie Francais des Pétroles, Notes et Memoires*, *18*, 35–44.

Sanay, R., Voulgaris, G., & Warner, J. C. (2007). Tidal asymmetry and residual circulation over linear sandbanks and their implication on sediment transport: A process-oriented numerical study. *Journal of Geophysical Research*, *112*, C12015. https://doi.org/10.1029/2007JC004101

Schuttelaars, H. M., & De Swart, H. E. (1996). An idealized long term morphodynamic model of a tidal embayment. *European Journal of Mechanics-B/Fluids*, *15*, 55.

Schuttelaars, H. M., & De Swart, H. E. (1999). Initial formation of channels and shoals in a short tidal embayment. *Journal of Fluid Mechanics*, *386*, 15–42. https://doi.org/10.1017/S0022112099004395

Scully, M. E., & Friedrichs, C. T. (2007). Sediment pumping by tidal asymmetry in a partially mixed estuary. *Journal of Geophysical Research*, *112*, C07028. https://doi.org/10.1029/2006JC003784

Scully, M. E., Geyer, W. R., & Lerczak, J. A. (2009). The influence of lateral advection on the residual estuarine circulation: A numerical modeling study of the Hudson River estuary. *Journal of Physical Oceanography*, *39*(1), 107–124. https://doi.org/10.1175/2008JPO3952.1

Seminara, G. (2010). Fluvial sedimentary patterns. *Annual Review of Fluid Mechanics*, *42*(1), 43–66. https://doi.org/10.1146/annurev-fluid-121108-145612

Shchepetkin, A. F., & McWilliams, J. C. (2005). The Regional Oceanic Modeling System (ROMS): A split-explicit, free-surface, topography-following-coordinate oceanic model. *Ocean Modelling*, *9*(4), 347–404. https://doi.org/10.1016/j.ocemod.2004.08.002

Sottolichio, A., Hanquiez, V., Périnotto, H., Sabouraud, L., & Weber, O. (2013). Evaluation of the recent morphological evolution of the Gironde estuary through the use of some preliminary synthetic indicators. In D. C. Conley, G. Masselink, P. E. Russell, & T. J. O'Hare (Eds.), *Proceedings 12th International Coastal Symposium* (Vol. 65, pp. 1224–1229). Plymouth, England: Journal of Coastal Research.

Soulsby, R. L., & Damgaard, J. S. (2005). Bedload sediment transport in coastal waters. *Coastal Engineering*, *52*(8), 673–689. https://doi.org/10.1016/j.coastaleng.2005.04.003

Stefanon, L., Carniello, L., DAlpaos, A., & Lanzoni, S. (2010). Experimental analysis of tidal network growth and development. *Continental Shelf Research*, *30*(8), 950–962. https://doi.org/10.1016/j.csr.2009.08.018

Stefanon, L., Carniello, L., D'Alpaos, A., & Rinaldo, A. (2012). Signatures of sea level changes on tidal geomorphology: Experiments on network incision and retreat. *Geophysical Research Letters*, *39*, L12402. https://doi.org/10.1029/2012GL051953

Tambroni, N., Bolla Pittaluga, M., & Seminara, G. (2005). Laboratory observations of the morphodynamic evolution of tidal channels and tidal inlets. *Journal of Geophysical Research*, *110*, F04009. https://doi.org/10.1029/2004JF000243

Tambroni, N., Luchi, R., & Seminara, G. (2017). Can tide dominance be inferred from the point bar pattern of tidal meandering channels? *Journal of Geophysical Research: Earth Surface*, *122*, 492–512. https://doi.org/10.1002/2016JF004139

Umlauf, L., & Burchard, H. (2003). A generic length-scale equation for geophysical turbulence models. *Journal of Marine Research*, *61*(2), 235–265. https://doi.org/10.1357/002224003322005087

Valle-Levinson, A., Reyes, C., & Sanay, R. (2003). Effects of bathymetry, friction and Earth's rotation on estuary/ocean exchange. *Journal of Physical Oceanography*, *33*(11), 2375–2393. https://doi.org/10.1175/1520-0485(2003)033<2375:EOBFAR>2.0.CO;2

Van der Wegen, M. (2013). Numerical modeling of the impact of sea level rise on tidal basin morphodynamics. *Journal of Geophysical Research: Earth Surface*, *118*, 447–460. https://doi.org/10.1002/jgrf.20034

Van der Wegen, M., Dastgheib, A., & Roelvink, J. A. (2010). Morphodynamic modelling of tidal channel evolution in comparison to empirical PA relationship. *Coastal Engineering*, *57*(9), 827–837. https://doi.org/10.1016/j.coastaleng.2010.04.003

Van der Wegen, M., & Roelvink, J. A. (2008). Long-term morphodynamic evolution of a tidal embayment using a two-dimensional, process-based model. *Journal of Geophysical Research*, *113*, C03016. https://doi.org/10.1029/2006JC003983

Van der Wegen, M., Wang, Z. B., Savenije, H. H. G., & Roelvink, J. A. (2008). Long-term morphodynamic evolution and energy dissipation in a coastal plain, tidal embayment. *Journal of Geophysical Research*, *113*, F03001. https://doi.org/10.1029/2007JF000898

Van Maanen, B., Coco, G., & Bryan, K. (2013). Modelling the effects of tidal range and initial bathymetry on the morphological evolution of tidal embayments. *Geomorphology*, *191*, 23–34. https://doi.org/10.1016/j.geomorph.2013.02.023

Van Maanen, B., Coco, G., & Bryan, K. (2015). On the ecogeomorphological feedbacks that control tidal channel network evolution in a sandy mangrove setting. *Proceedings of the Royal Society*, *471*(2180). https://doi.org/10.1098/rspa.2015.0115

Van Maanen, B., Coco, G., Bryan, K. R., & Friedrichs, C. T. (2013). Modeling the morphodynamic response of tidal embayments to sea-level rise. *Ocean Dynamics*, *63*(11–12), 1249–1262. https://doi.org/10.1007/s10236-013-0649-6

Vlaswinkel, B. M., & Cantelli, A. (2011). Geometric characteristics and evolution of a tidal channel network in experimental setting. *Earth Surface Processes and Landforms*, *36*(6), 739–752. https://doi.org/10.1002/esp.2099

Warner, J. C., Sherwood, C. R., Arango, H. G., & Signell, R. P. (2005). Performance of four turbulence closure models implemented using a generic length scale method. *Ocean Modelling*, *8*(1), 81–113.

Warner, J. C., Sherwood, C. R., Signell, R. P., Harris, C. K., & Arango, H. G. (2008). Development of a three-dimensional, regional, coupled wave, current, and sediment-transport model. *Computers & Geosciences*, *34*(10), 1284–1306. https://doi.org/10.1016/j.cageo.2008.02.012

Wong, K.-C. (1994). On the nature of transverse variability in a coastal plain estuary. *Journal of Geophysical Research*, *99*(C7), 14,209–14,222. https://doi.org/10.1029/94JC00861

Wright, L., Coleman, J., & Thom, B. (1973). Processes of channel development in a high-tide-range environment: Cambridge Gulf-Ord River delta, Western Australia. *Journal of Geology*, *81*(1), 15–41. https://doi.org/10.1086/627805

Zhou, Z., Coco, G., Jiménez, M., Olabarrieta, M., van der Wegen, M., & Townend, I. (2014). Morphodynamics of river-influenced back-barrier tidal basins: The role of landscape and hydrodynamic settings. *Water Resources Research*, *50*, 9514–9535. https://doi.org/10.1002/2014WR015891

Zhou, Z., Coco, G., Townend, I., Olabarrieta, M., Van der Wegen, M., Gong, Z., et al. (2017). Is "Morphodynamic equilibrium" an oxymoron? *Earth-Science Reviews*, *165*, 257–267. https://doi.org/10.1016/j.earscirev.2016.12.002